Impact of CASA Radar and Oklahoma Mesonet Data Assimilation on the Analysis and Prediction of Tornadic Mesovortices in an MCS

ALEXANDER D. SCHENKMAN, MING XUE, AND ALAN SHAPIRO

Center for Analysis and Prediction of Storms, and School of Meteorology, University of Oklahoma, Norman, Oklahoma

KEITH BREWSTER

Center for Analysis and Prediction of Storms, Norman, Oklahoma

JIDONG GAO

National Severe Storms Laboratory, Norman, Oklahoma

(Manuscript received 21 November 2010, in final form 16 February 2011)

ABSTRACT

The impact of radar and Oklahoma Mesonet data assimilation on the prediction of mesovortices in a tornadic mesoscale convective system (MCS) is examined. The radar data come from the operational Weather Surveillance Radar-1988 Doppler (WSR-88D) and the Engineering Research Center for Collaborative Adaptive Sensing of the Atmosphere's (CASA) IP-1 radar network. The Advanced Regional Prediction System (ARPS) model is employed to perform high-resolution predictions of an MCS and the associated cyclonic line-end vortex that spawned several tornadoes in central Oklahoma on 8–9 May 2007, while the ARPS three-dimensional variational data assimilation (3DVAR) system in combination with a complex cloud analysis package is used for the data analysis. A set of data assimilation and prediction experiments are performed on a 400-m resolution grid nested inside a 2-km grid, to examine the impact of radar data on the prediction of meso-γ-scale vortices (mesovortices). An 80-min assimilation window is used in radar data assimilation experiments. An additional set of experiments examines the impact of assimilating 5-min data from the Oklahoma Mesonet in addition to the radar data.

Qualitative comparison with observations shows highly accurate forecasts of mesovortices up to 80 min in advance of their genesis are obtained when the low-level shear in advance of the gust front is effectively analyzed. Accurate analysis of the low-level shear profile relies on assimilating high-resolution low-level wind information. The most accurate analysis (and resulting prediction) is obtained in experiments that assimilate low-level radial velocity data from the CASA radars. Assimilation of 5-min observations from the Oklahoma Mesonet has a substantial positive impact on the analysis and forecast when high-resolution low-level wind observations from CASA are absent; when the low-level CASA wind data are assimilated, the impact of Mesonet data is smaller. Experiments that do not assimilate low-level wind data from CASA radars are unable to accurately resolve the low-level shear profile and gust front structure, precluding accurate prediction of mesovortex development.

1. Introduction

Because most tornadoes are spawned by supercells, the majority of modeling and data assimilation studies that analyze or simulate tornadic systems have focused on supercellular cases (e.g., Klemp et al. 1981; Klemp and Rotunno 1983; Rotunno 1993; Wicker and Wilhelmson 1995; Dowell et al. 2004; Sun 2005; Hu et al. 2006a). A climatology presented in Trapp et al. (2005) suggests that ~20% of tornado cases in the United States were spawned by quasi-linear convective systems such as bow echoes and squall lines. That tornadoes sometimes occur in association with bow echoes and their associated line-end vortices (LEV; Weisman 1993; Skamarock et al. 1994; Weisman and Davis 1998) has also been noted in many studies (e.g., Forbes and Wakimoto 1983; Przybylinski 1995; Pfost and Gerard

Corresponding author address: Alex Schenkman, School of Meteorology, University of Oklahoma, 120 David L. Boren Blvd., Norman, OK 73072.
E-mail: alex3238@ou.edu

DOI: 10.1175/MWR-D-10-05051.1

1997; Weisman and Trapp 2003; Davis et al. 2004). In this study, we employ high-resolution data assimilation and modeling to analyze and simulate a mesoscale convective system (MCS) and associated LEV that spawned at least 5 tornadoes in central Oklahoma on 8–9 May 2007.

In Schenkman et al. (2011, hereafter S11), the mesoscale evolution of the 8–9 May 2007 MCS and associated cyclonic LEV was well reproduced at 2-km horizontal resolution in model forecasts that assimilated data from multiple Weather Surveillance Radar-1988 Doppler (WSR-88D) radars. Further improvement was realized when additional radial velocity data from the Engineering Research Center (ERC) for Collaborative Adaptive Sensing of the Atmosphere's (CASA) IP-1 X-band radar network (see McLaughlin et al. 2009 and S11) were assimilated. These improvements were mainly manifested in the analysis of the MCS's gust front structure and location. The improved gust front structure led to a slightly more accurate track forecast of the LEV associated with the MCS.

In the present study, we nest a 400-m resolution grid within the 2-km grid used in S11. This enhanced resolution allows us to take advantage of the high-spatial-resolution observations of the CASA radars. As on the 2-km grid of S11, data are analyzed on the 400-m grid using high-frequency analysis cycles over an assimilation window. Additionally, by increasing the resolution we examine whether the model is able to capture substorm-scale features, particularly the observed low-level tornadic meso-γ-scale (Orlanski 1975) vortices (hereafter mesovortices).

The tendency of MCSs and associated mesovortices to produce tornadoes has been well documented (e.g., Forbes and Wakimoto 1983; Przybylinski 1995; Atkins et al. 2004; Davis et al. 2004; Wakimoto et al. 2006b; Atkins and Laurent 2009b). Fujita (1978) presented a conceptual model of the life cycle of bow-echoes and associated LEVs. His schematic suggested that tornadoes in MCSs are most likely to form just north of the apex of the bow echo as well as at the tip of the comma echo associated with the cyclonic LEV.

More recent studies have highlighted the role of subsystem-scale mesovortices in spawning both damaging winds and tornadoes (e.g., Przybylinski 1995; Funk et al. 1999; Atkins et al. 2004, 2005; Wakimoto et al. 2006a,b). Atkins et al. (2004, 2005) show that tornadic mesovortices are longer lived and intensify more rapidly than their nontornadic counterparts. Additionally, the mean tornado lifetime was substantially shorter than that of the parent mesovortex.

Quasi-idealized modeling studies of Weisman and Trapp (2003) and Atkins and St. Laurent (2009a) indicate that mesovortices form in the strong equivalent potential temperature θ_e gradient of a thunderstorm outflow and are longer lived and more intense in the presence of stronger low to midlevel shear. These studies explain that larger shear values allow for more upright convective cells, creating a more favorable environment for the amplification and maintenance of mesovortices through the stretching of vorticity. Thus, we hypothesize that an accurate analysis and/or forecast of the low-level shear profile (and other related features, such as, the cold pool and gust front location and evolution) in the vicinity of developing mesovortices is paramount in forecasting the intense, long-lived tornadic mesovortices observed in the 8–9 May 2007 case. We attempt to verify our hypothesis through a set of experiments that assimilate real observations. To our knowledge, our study is the first to try predicting mesovortex development within a mesoscale convective system by assimilating real Doppler radar data. It is also one of the first studies focusing on examining the impact of experimental CASA radar data on the prediction of storm-scale as well as substorm-scale features.

This paper is organized as follows. In section 2, an overview of the mesovortices of the 8–9 May 2007 case is presented. Section 3 describes the design of the numerical experiments and section 4 discusses the results from a set of experiments that examine the impact of assimilated CASA data on the prediction of our case. Section 5 describes additional experiments designed to investigate the impact of assimilating 5-min frequency wind and thermodynamic data from the Oklahoma Mesonet. A summary and conclusions are given in section 6.

2. Case overview

An MCS and associated LEV produced several weak tornadoes that struck parts of southwest and central Oklahoma on 9 May 2007. According to a National Weather Service (NWS) damage survey, the first tornado caused EF-1 damage in Grady County, near Minco, Oklahoma. Another weak tornado produced EF-0 damage near Union City, Oklahoma, in Canadian County. The most destructive tornado, a high-end EF-1, hit El Reno, Oklahoma, causing an estimated $3 million (U.S. dollars) of damage. Two very short-lived EF-1 tornadoes were reported near Piedmont a short time after the El Reno tornado. Figure 1 shows a map with the above referenced locations.

Examination of radial velocity observations of the 9 May 2007 MCS and LEV from the Oklahoma City (KOKC) Terminal Doppler Weather Radar (TDWR) over the period 0300–0500 UTC reveals at least 5 distinct mesovortices. All of the mesovortices developed during the comma echo stage of the MCS to the east and southeast of the LEV. The mesovortices generally moved

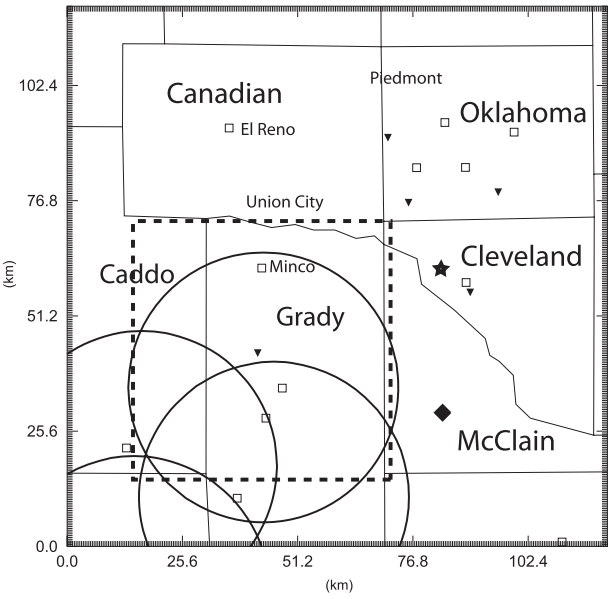

FIG. 1. Map of the 400-m horizontal-resolution model domain used in this study. Selected county and city names are indicated. The small squares represent locations of assimilated Oklahoma Mesonet sites. The filled triangles are locations of assimilated ASOS sites and the filled diamond is the location of the Purcell profiler. The circles (and arcs) represent the maximum range (30 km) of the CASA IP1 radars. The dashed-line rectangle marks the area plotted in Fig. 2. The star in Cleveland County marks the location of the KOKC TDWR.

north and west, rotating around the LEV. Radar reflectivity observations indicate that the mesovortices were associated with strong convective cells embedded within the comma echo. As the mesovortices intensified, the associated convective cells briefly took on a supercellular appearance with a hook echo becoming apparent (not shown). This is especially true for the mesovortex that spawned the Minco tornado. Weisman and Trapp (2003) also noted the supercellular appearance of convective cells associated with mesovortices. However, they show that there are large structural and dynamical differences between a supercell and convective cells associated with mesovortices. Namely, the mesovortex is not associated with a deep-rotating midlevel updraft and thus lacks the dynamically forced vertical accelerations associated with supercell mesocyclones.

Of the five mesovortices that developed in the 8–9 May 2007 MCS, only two were tornadic. These two were longer-lived than the nontornadic mesovortices (Table 1). Both the Minco and Union City tornadoes appeared to form in association with the same mesovortex (hereafter the Minco mesovortex). Figure 2 shows the evolution of the Minco mesovortex in terms of the radial velocity observations of KOKC radar. These observations show that the Minco mesovortex is initially the weaker

TABLE 1. List of the mesovortices, their lifetime (as determined from TDWR data) and whether they were associated with tornadoes (determined from storm damage reported time/locations compared with TDWR observations).

Mesovortex	Lifetime (min)	Tornadic (yes–no)
Mesovortex No. 1	40	No
Minco mesovortex	70	Yes
Mesovortex No. 3	20	No
Mesovortex No. 4	30	No
El Reno mesovortex	65	Yes

and broader circulation among a pair of mesovortices at 0300 UTC (Fig. 2a). As the Minco mesovortex strengthens, its diameter (determined by the approximate distance between peak inbound and outbound velocities in the radial velocity Vr data) decreases from around 6–7 to 3–4 km (Figs. 2b,c). The Minco mesovortex begins to weaken around 0400 UTC (Fig. 2d).

The mesovortex associated with the El Reno tornado (hereafter the El Reno mesovortex) formed immediately after the dissipation of the Union City tornado. The El Reno mesovortex is larger and stronger than the earlier mesovortices and was associated with an area of strong convergence on its eastern side with >30 m s^{-1} inflow. The El Reno tornado developed on the northwest side of the convergence zone and moved west relative to the convergence zone. The El Reno mesovortex and convergence zone persist after the dissipation of the El Reno tornado and spawns the two brief Piedmont tornadoes. Owing to the expected limit of predictability, our study only focuses on the mesovortices associated with the first three tornadoes (i.e., the Minco and El Reno mesovortices).

3. Experiment design and verification procedure

a. Grid and data analysis configurations

The primary research tool for our analysis is the ARPS prediction model (Xue et al. 2000, 2001) and its three-dimensional variational data assimilation (3DVAR) and cloud-analysis packages (Xue et al. 2003; Gao et al. 2004; Hu et al. 2006a,b). The data assimilation and forecast experiments are conducted on a 400-m horizontal-resolution grid 120×120 km^2 in size centered at 35.25°N, 97.80°W (Fig. 1). The grid covers a portion of southwest and central Oklahoma and is one-way nested within the 2-km resolution grid that is 1000×1000 km^2 in size and centered at 34.80°N, 98.00°W. This 2-km grid covers all of Oklahoma, the northern half of Texas, southern Kansas, and far southeastern Colorado (see Fig. 3 of S11). We point out here the computational constraints limited the coverage of the 400-m resolution grid to

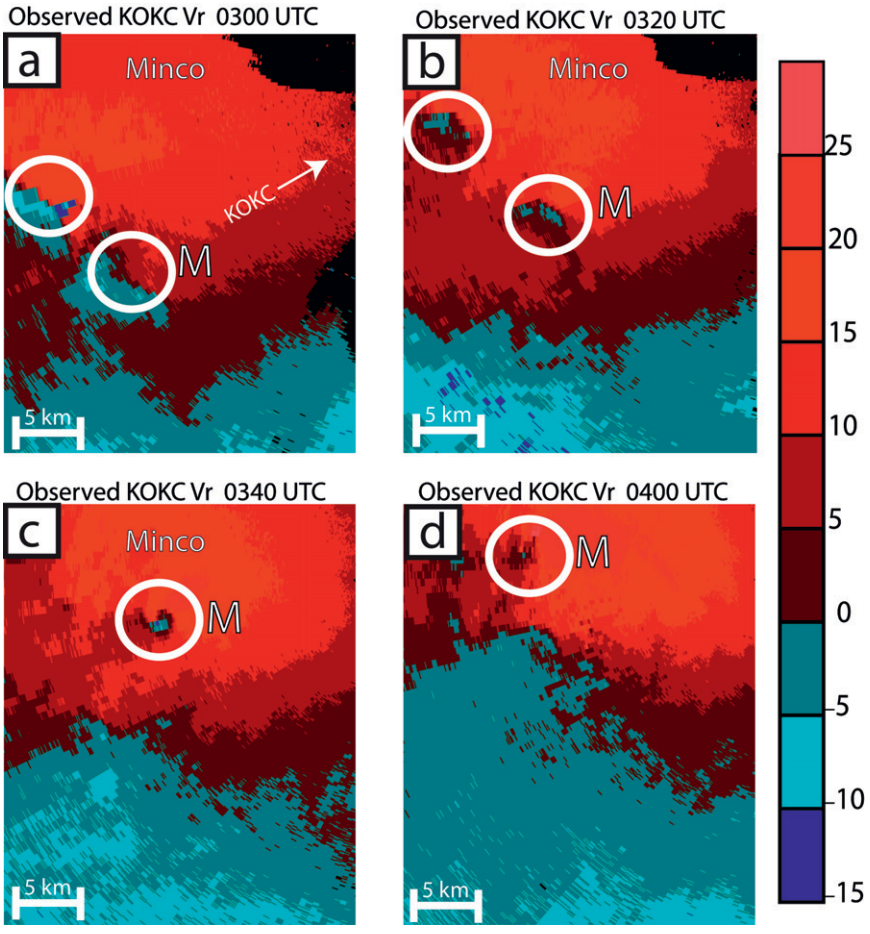

FIG. 2. Evolution of the Minco mesovortex as observed by the KOKC TDWR at (a) 0300, (b) 0320, (c) 0340, and (d) 0400 UTC 9 May 2007. Fields are plotted over the area marked by the dashed line rectangle in Fig. 1. The white circles have a diameter of 6 km and identify mesovortices. Circles annotated with the ''M'' indicate the Minco mesovortex. Black shading represents missing data. KOKC is located ~30 km in the direction of the white arrow in from the KOKC in (a). The location of Minco is indicated in (a)–(c).

include only the northeastern three quarters of the CASA IP-1 domain (see Fig. 1); the Advanced Regional Prediction System (ARPS) 3DVAR system used in this study did not support distributed parallel processing early on. Still, this 400-m grid does include nearly all of multi-Doppler coverage area of the CASA IP-1 network and the most important small-scale features that developed along the gust fronts were within the 400-m grid during the later data assimilation cycles. Equally important is that this grid provides sufficient coverage downstream of the CASA domain to allow the forecast MCS and LEV to evolve within the grid during the time period of interest. Furthermore, the 400-m resolution grid does benefit from high-frequency data assimilation performed on the 2-km resolution grid, whose information can be propagated into the 400-m resolution grid through the upstream boundaries. The 400-m grid is stretched in the vertical, with a minimum vertical resolution of 100 m near the surface. Grid stretching is calculated according to a cubic function of height as documented in the ARPS user's guide (Xue et al. 1995). There are 63 vertical levels on the 400-m grid, while the 2-km grid had 43 levels.

The ARPS 3DVAR and cloud analysis combination is used for data assimilation in this study. 3DVAR is used in this study as an alternative to the more advanced four-dimensional variational data assimilation (4DVAR) data assimilation method because no general storm-scale 4DVAR with ice microphysics exists. To enable direct comparison of ensemble Kalman filter (EnKF) with 3DVAR a parallel study is under way using EnKF for the same case (Snook et al. 2011). As described in S11, ARPS 3DVAR is designed to perform multiple analysis passes with different recursive filter scales

TABLE 2. List of assimilated data types and 3DVAR analysis properties.

Data source	Analysis pass	Horizontal decorrelation radius (km)	Vertical decorrelation radius (grid points)	Assimilation frequency
Profiler	1	50.0	4	Hourly
ASOS	2	30.0	4	Hourly
Oklahoma Mesonet	2	30.0	4	Hourly–5 min*
MDCRS	2	30.0	4	Hourly
WSR-88D	3	0.8	2	5 min
CASA IP-1	3	0.8	2	5 min

* Mesonet data are assimilated hourly or every 5 min depending on the experiment.

(corresponding to background error decorrelation scales) in order to account for the significant differences in the observation network spacings and the scales that these networks observe (Xue et al. 2003; Gao et al. 2004). For our purposes, we use three analysis passes with a decreasing filter scale on each pass. Upper-air data from wind profilers are analyzed in the first analysis pass with a horizontal decorrelation scale of 50 km, because these data have the coarsest horizontal resolutions. Surface wind and thermodynamic observations from the Automated Surface Observing System (ASOS) and Oklahoma Mesonet as well as aircraft observations are analyzed in the second analysis pass with a horizontal decorrelation scale of 30 km. The vertical decorrelation scale is 4 grid intervals in both passes.

Radar radial velocity data are used in the third analysis pass. Level-II data are used from two WSR-88D radars: Twin Lakes (KTLX) and Vance (KVNX). In experiments utilizing CASA data, data from all four CASA IP-1 radars [Chickasha (KSAO), Cyril (KCYR), Lawton (KLWE), and Rush Springs (KRSP)] are used. For these dense radar data, the horizontal decorrelation scale is set to 0.8 km and the vertical scale is reduced to 2 grid intervals. Table 2 summarizes the analysis parameters for the various data sources. Specified observational error covariance for all assimilated data types are presented in Table 3. The radar reflectivity data are used in the cloud analysis package as an additional step following the 3DVAR analysis. Other details on the analysis procedure, including radar data processing, and specifics on the cloud analysis package, are the same as those used on the 2-km grid; interested readers are referred to S11.

b. Experiment design

Our experiments in this study are designed to focus on the impacts of various data sources. As described in S11, a 1-hr ''spinup'' forecast was first performed from 0000–0100 UTC on the 2-km grid starting from an interpolated 0000 UTC NAM analysis. This 1-h forecast is interpolated to the 400-m grid to provide an initial analysis background for the data assimilation cycles. Lateral boundary conditions for the 400-m grid are obtained from the matching forecasts on the 2-km grid, at 5-min intervals (see the second column of Table 4).

High-frequency, 5-min interval, intermittent analysis cycles start at 0100 UTC 9 May 2007. These cycles end at 0220 UTC, which extends 20 min longer than the 60-min-long assimilation window used by the 2-km radar data assimilating experiments reported in S11. The 20-min window extension is performed to ensure that several data assimilation cycles take place when features of interest (e.g., the gust front and cold pool) are fully within the 400-m domain. Forecasts are launched from the final analysis and run up to 0500 UTC 9 May 2007.

The experiments differ based upon the observational data they assimilate. With the exception of one experiment that assimilates no radar data (NORAD), all experiments assimilate both radial velocity Vr and reflectivity Z data from the WSR-88D radars listed in section 3a. To examine the impact of CASA data, additional experiments assimilate WSR-88D data together with CASA Vr data only (CASAVr), CASA Z data only (CASAZ), and both CASAVr and Z (CASAVrZ) data. Experiment 88DONLY uses radar data from the WSR-88D network only.

TABLE 3. Specified observation error covariance values for all assimilated data types. If a range of values is given it refers to the specified error variance from the near surface to the highest altitude observation.

Data source	u (m s^{-1})	v (m s^{-1})	Pressure (hPa)	Temperature (K)	Relative humidity (%)
Profiler	2.0–3.5	2.0–3.5	0.6–0.4	1.0–2.0	13–20
MDCRS	1.5	1.5	1.22	1.11	10.0
ASOS	1.0	1.0	2.00	0.60	5.0
OK Mesonet	1.5	1.5	2.00	1.11	5.0
Data source	Radial velocity (m s^{-1})				
WSR-88D	2.0				
CASA IP-1	2.5				

TABLE 4. List of experiments and some of their key parameters. The column "LBC source" lists the 2-km experiment from S11 that provides lateral boundary conditions to the corresponding 400-m experiment.

Expt name	LBC source	5-min OK Mesonet data	WSR-88D Vr data	WSR-88D *Z* data	CASA *Z* data	CASA Vr data
88DONLY	88DONLY	No	Yes	Yes	No	No
CASAVrZ	CASAVrZ	No	Yes	Yes	Yes	Yes
CASAVr	CASAVr	No	Yes	Yes	No	Yes
CASAZ	CASAZ	No	Yes	Yes	Yes	No
NORAD	NORAD	No	No	No	No	No
CASAVrZ5MM	CASAVrZ	Yes	Yes	Yes	Yes	Yes
CASAZ5MM	CASAZ	Yes	Yes	Yes	Yes	No

The above experiments also assimilate Oklahoma Mesonet wind and thermodynamic data, but only at 0100 and 0200 UTC. To further explore the potential of Oklahoma Mesonet data, two additional experiments are performed that assimilate 5-min Oklahoma Mesonet data. Experiment CASAVrZ5MM (CASAZ5MM) is identical to experiment CASAVrZ (CASAZ), except 5-min Mesonet observations are assimilated. CASAVrZ5MM intends to examine if 5-min Mesonet data can provide benefit in addition to CASA observations (in this case) while CASAZ5MM intends to determine whether the Mesonet observations assimilated at the same frequency as CASA data can replace CASAVr observations in terms of their impact on the low-level wind analysis. WSR-88D radar data are assimilated in all experiments that assimilated CASA data, because such data are routinely available in the region. In regions where only CASA-type dense radars are available, we expect even greater impacts. Configurations from all experiments are summarized in Table 4. Results from these experiments will be discussed in sections 4 and 5.

4. Impact of CASA observations

In this section, we examine the impact of assimilating CASA observations on the analysis and prediction of the low-level kinematic and thermodynamic fields (i.e., the cold pool, gust front, and mesovortices). We expect that (as was shown in S11) the assimilation of CASA reflectivity data in addition to WSR-88D reflectivity data will have little impact on the quality of the analysis and forecast. As such, we split the radar-assimilating experiments into two categories: those that assimilate high-resolution low-level wind (LLW) information from the CASA radars (hereafter LLW experiments) and those that do not [hereafter no low-level wind (NLLW) experiments]. The LLW experiments consist of CASAVrZ and CASAVr while the NLLW experiments are made up of 88DONLY and CASAZ. NORAD is also a NLLW experiment; however, it is discussed separately at the end of this section because it is the only experiment that does not assimilate radar data. Experiments CASAVrZ5MM and CASAZ5MM belong to the LLW and NLLW experiment groups, respectively, but they examine the impact of high-frequency mesonet data and are discussed separately in section 5.

In section 4b, we discuss the development and evolution of simulated mesovortices. For our purposes, a simulated circulation is considered a mesovortex if its maximum vorticity exceeds 0.025 s^{-1} for 15 min or more. The vorticity criterion is based on Weisman and Trapp (2003) multiplied by a factor of 2.5 to account for the resolution differences between their study and ours [Weisman and Trapp (2003) used a criterion of 0.01 s^{-1} for their 1-km grid spacing, whereas our study uses 400-m grid spacing). The temporal criterion is designed to avoid classifying short-lived (~5 min) intense shear zones as mesovortices.

In this paper, we will also refer to weak, moderate, and strong low-level shear. For our purposes, we define low-level shear as the magnitude of the change in the *u* (east–west velocity) component of total velocity over the lowest 2.5 km of the model domain. The *u* component is examined because it is roughly perpendicular to the gust front in areas of greatest interest and makes for a more straightforward comparison with Weisman and Trapp (2003) and Atkins and St. Laurent (2009a) because those studies examined the impact of unidirectional shear on mesovortex formation, strength, and longevity. Following Weisman and Trapp (2003), we define weak, moderate, and strong shears as those with 2.5-km *u* differences of 0–10, 10–20, and greater than 20 m s^{-1}, respectively. A positive (or negative) designation refers to the magnitude of u increasing (or decreasing) with height.

a. Analyses at the end of assimilation window, 0220 UTC

The most pronounced differences between the LLW and NLLW experiments in the analyses at 0220 UTC, the end of data assimilation widow, are present in low-level cold-pool structure and gust front position (Fig. 3). Specifically, the primary gust front (i.e., the main gust

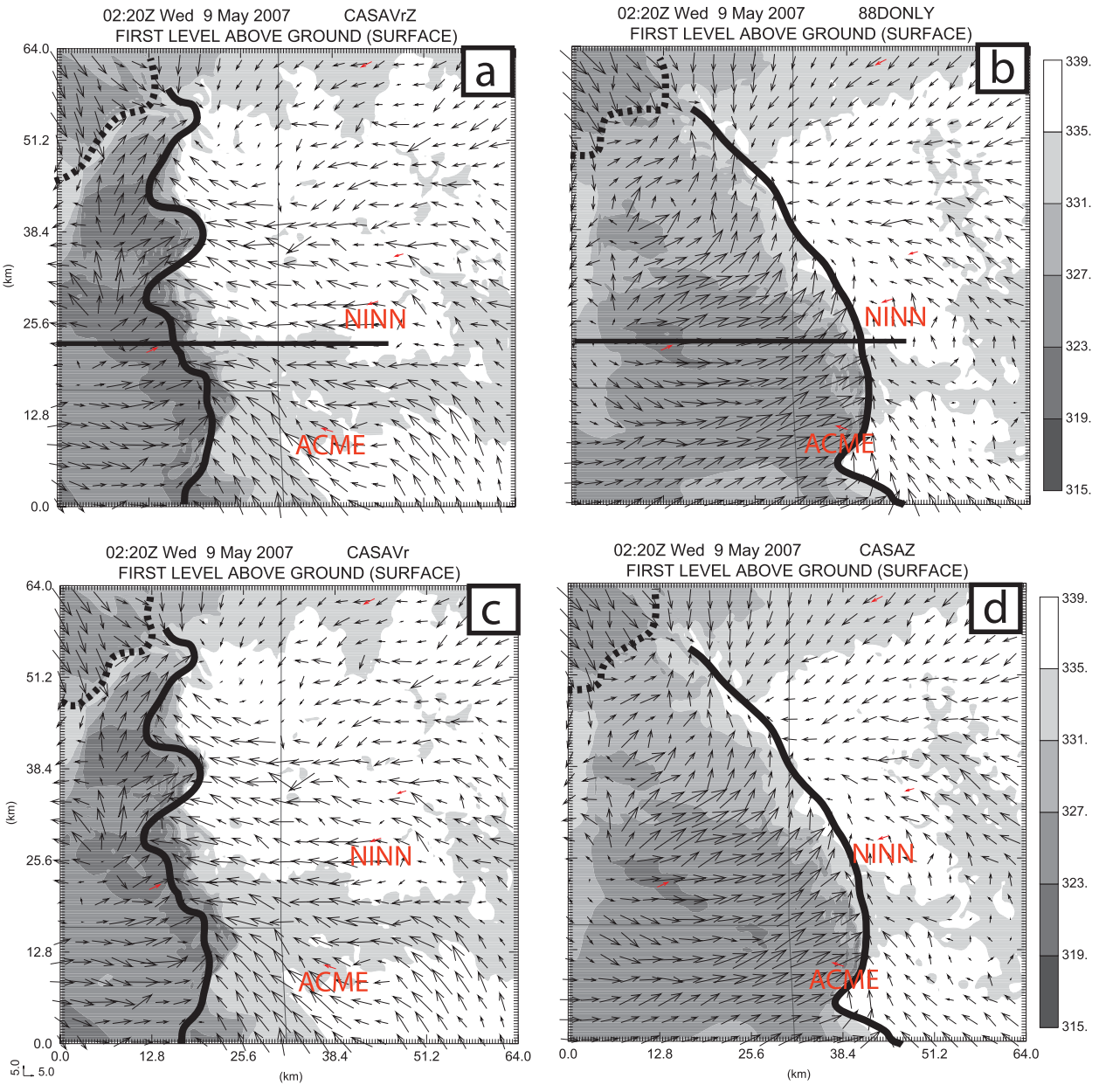

FIG. 3. The 0220 UTC 9 May 2007 near-surface analysis from experiments (a) CASAVrZ, (b) 88DONLY, (c) CASAVr, and (d) CASAZ. Equivalent potential temperature is shaded gray at 4-K intervals, vectors are for horizontal winds (m s^{-1}), and red bold vectors are for mesonet wind observations (m s^{-1}). The heavy black line represents the approximate location of the primary gust front. The horizontal black line near $y = 23.0$ km in (a) and (b) marks the location of the cross section in Fig. 6. The secondary outflow and gust front (marked by the heavy dashed line) is in the far upper-left corner in (a)–(d). The Acme and Ninnekah mesonet sites are annotated.

front of the system forced by downdrafts in the squall-line portion of the MCS) in the LLW experiments (Figs. 3a,c) is about 20 km farther west than it is in the NLLW experiments (Figs. 3b,d). Comparison with Oklahoma Mesonet 10-m wind observations (shown in Fig. 3) suggests that the gust front location in the LLW experiments is more accurate as, for example, the NLLW experiments indicate strong westerly flow behind the gust front where observations from the Acme, Oklahoma, mesonet site show inflow winds from the east. Further comparison with time series plots of observed potential temperature θ from the Acme and Ninnekah, Oklahoma, mesonet sites (Fig. 4) shows a much more accurate temporal evolution of θ in the LLW experiments than in the NLLW experiments. This indicates the gust front has advanced too far to the east in

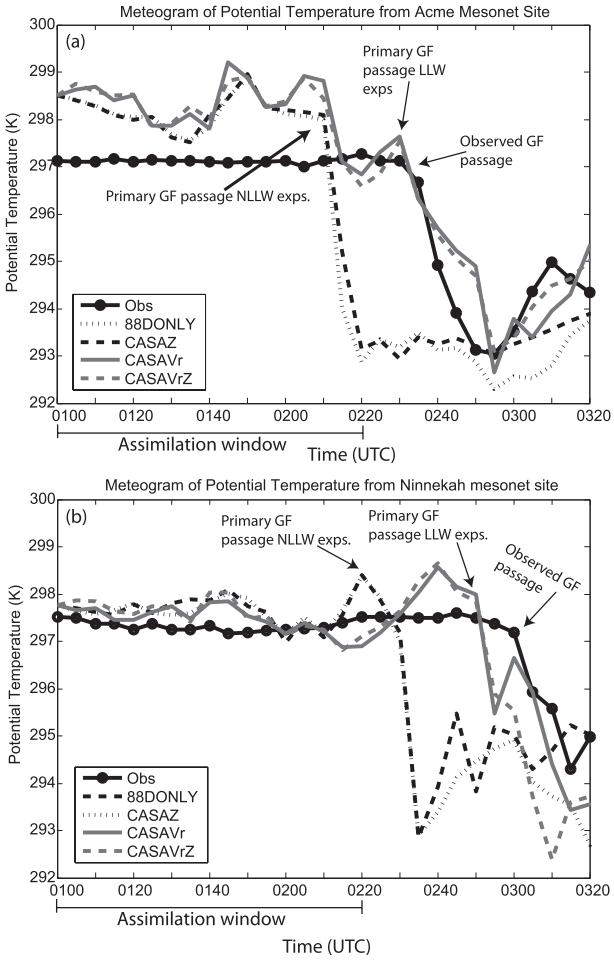

FIG. 4. Meteogram of potential temperature (K) observed and simulated at the (a) Acme and (b) Ninnekah mesonet sites from 0100–0320 UTC 9 May 2007. The gust front passage (GF) is noted for the NLLW and LLW experiments as well for the observations.

the NLLW experiments. Both the LLW and NLLW experiments feature a secondary gust front associated with another area of outflow to the northwest of the primary gust front. The secondary gust front enters the 400-m resolution domain from the 2-km resolution grid through the western lateral boundary around 0200 UTC (not shown). All experiments assimilate the same data in vicinity of the secondary gust front because it is outside of the CASA domain. Thus, the position of the secondary gust front is similar in all experiments. We also note here that the 0220 UTC analysis from CASAZ is nearly identical to that of 88DONLY and the 0220 UTC analysis from CASAVrZ is nearly identical to that of CASAVr, confirming our expectation that assimilating CASA reflectivity would have little impact on the analysis.

The position differences of the primary gust front between the LLW and NLLW experiments are caused by the ability (or inability) of the assimilated data sources to observe the low-level inflow field ahead of the gust front. The low-level outflow behind the gust front behaves like a density current. Xu et al. (1996) used a simplified, two-dimensional version of the ARPS model to examine density currents in a sheared environment. By specifying density current depth to be greater or less than the theoretical depth for a given shear [calculated based on the model developed in Xu (1992)], Xu et al. (1996) found that a density current with an overspecified (underspecified) depth would surge (retreat) and flatten (deepen) before reaching a quasi-steady state with a depth and propagation speed close to the values derived from Xu (1992). This density current behavior shows the great importance of low-level shear on density current depth and propagation and Xu et al. (1996) emphasize that ''quasi-steady solutions are controlled solely by the inflow shear'' and a stronger shear in the direction of density current propagation supports a deeper and stronger density current. Similar results are found for density currents in environments with nonconstant vertical shear by Xue et al. (1997). Their results are generally consistent with the view of Rotunno et al. (1988) that discusses the importance of low-level shear in supporting deep, upright updrafts in squall lines.

In the LLW experiments, the analyzed easterly near-surface inflow ahead of the primary gust front leads to generally moderate to strong positive low-level shear at and to the east of the gust front during assimilation window (Figs. 5a,c). In contrast, the NLLW experiments that do not assimilate low-level wind observations from CASA do not analyze the easterly near-surface inflow as accurately. Instead, the analyzed near-surface winds are from the south and southwest with weak southeasterly flow farther above the surface. As a result, the low-level shear in the direction of gust front propagation at and to the east of the primary gust front is generally weak and negative in the NLLW experiments during the assimilation window (Figs. 5b,d). Applying the results of density currents from Xu et al. (1996) to the experiments presented here, one would expect the cold pool to be deeper and move more slowly (relative to the ground) in the LLW experiments than the cold pool in the NLLW experiments. Examination of the cold-pool behavior in LLW and NLLW experiments confirms this expectation as during each forecast step of the analysis cycles within the assimilation window, the gust front surges eastward and flattens in the NLLW experiments but makes only slight eastward progress with little change in depth in the LLW experiments. The aggregate effect of these differences in the forecast steps is the 20-km difference in gust front position between the LLW and NLLW experiments at the end of the assimilation window at

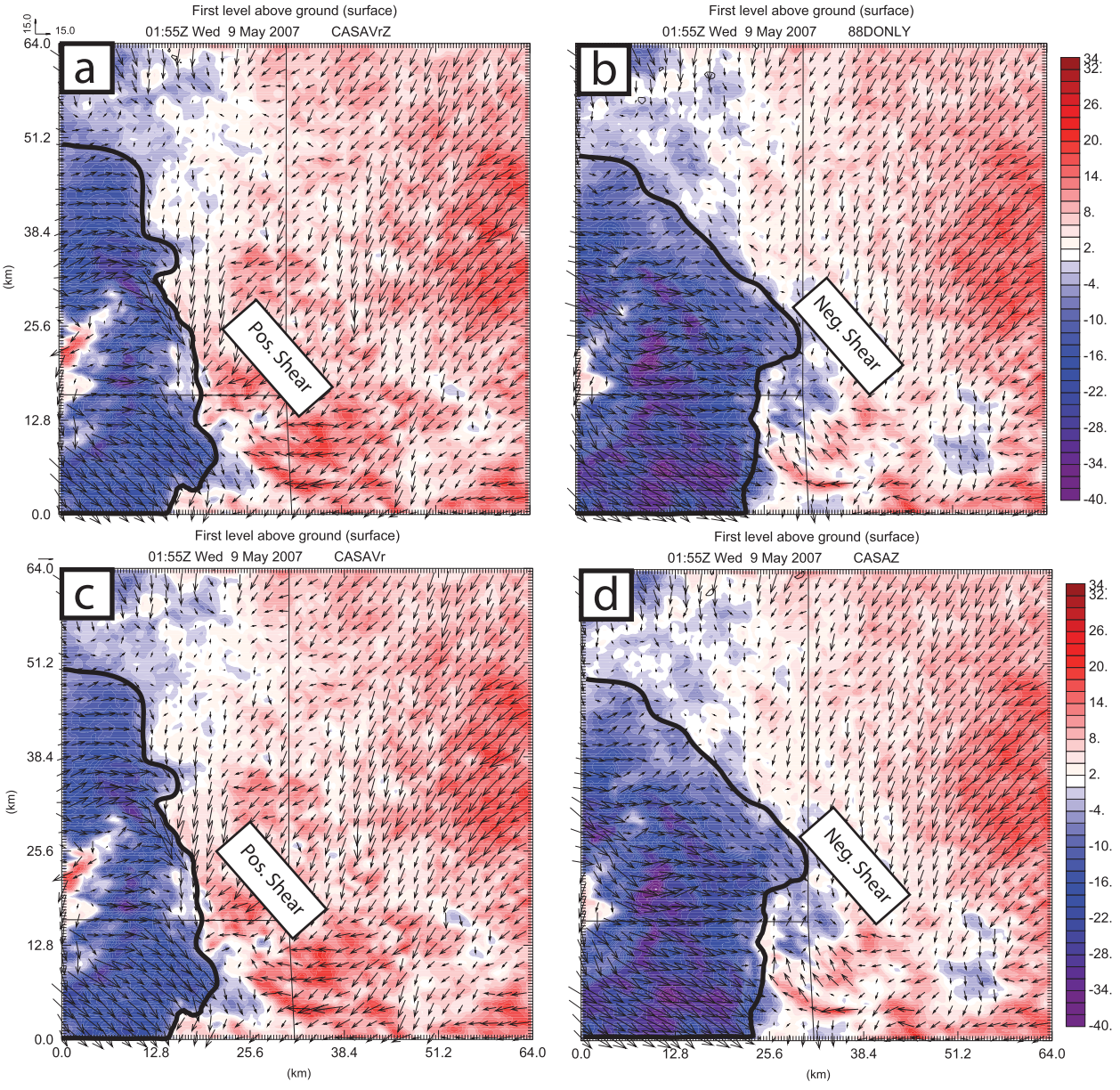

FIG. 5. Near-surface to 2.5 km AGL difference in magnitude of u-component velocity (shaded, m s^{-1}) and negative total velocity shear vectors (m s^{-1}) at 0155 UTC 9 May 2007 from (a) CASAVrZ, (b) 88DONLY, (c) CASAVr, and (d) CASAZ. The heavy black curve marks the approximate location of the gust front.

0220 UTC. An example of the differences in cold pool structure and propagation between the LLW and NLLW experiments is shown in Fig. 6 for CASAVrZ and 88DONLY. Note that the much deeper cold pool in CASAVrZ remains nearly stationary in the 5-min forecast step shown in Fig. 6, while over the same period in 88DONLY the shallow cold pool advances eastward by about 5 km and becomes even shallower in its leading portion. There is a much stronger easterly component in the flow ahead of the gust front at the low levels in CASAVrZ, which supports a deeper and stronger cold pool, and helps to hold back the gust front.

b. *Forecast results*

The differences in the analyzed gust front structure and location between the LLW and NLLW experiments lead to substantial differences in the evolution of substorm-scale mesovortices during the forecast period. These differences are most pronounced before 0400 UTC.

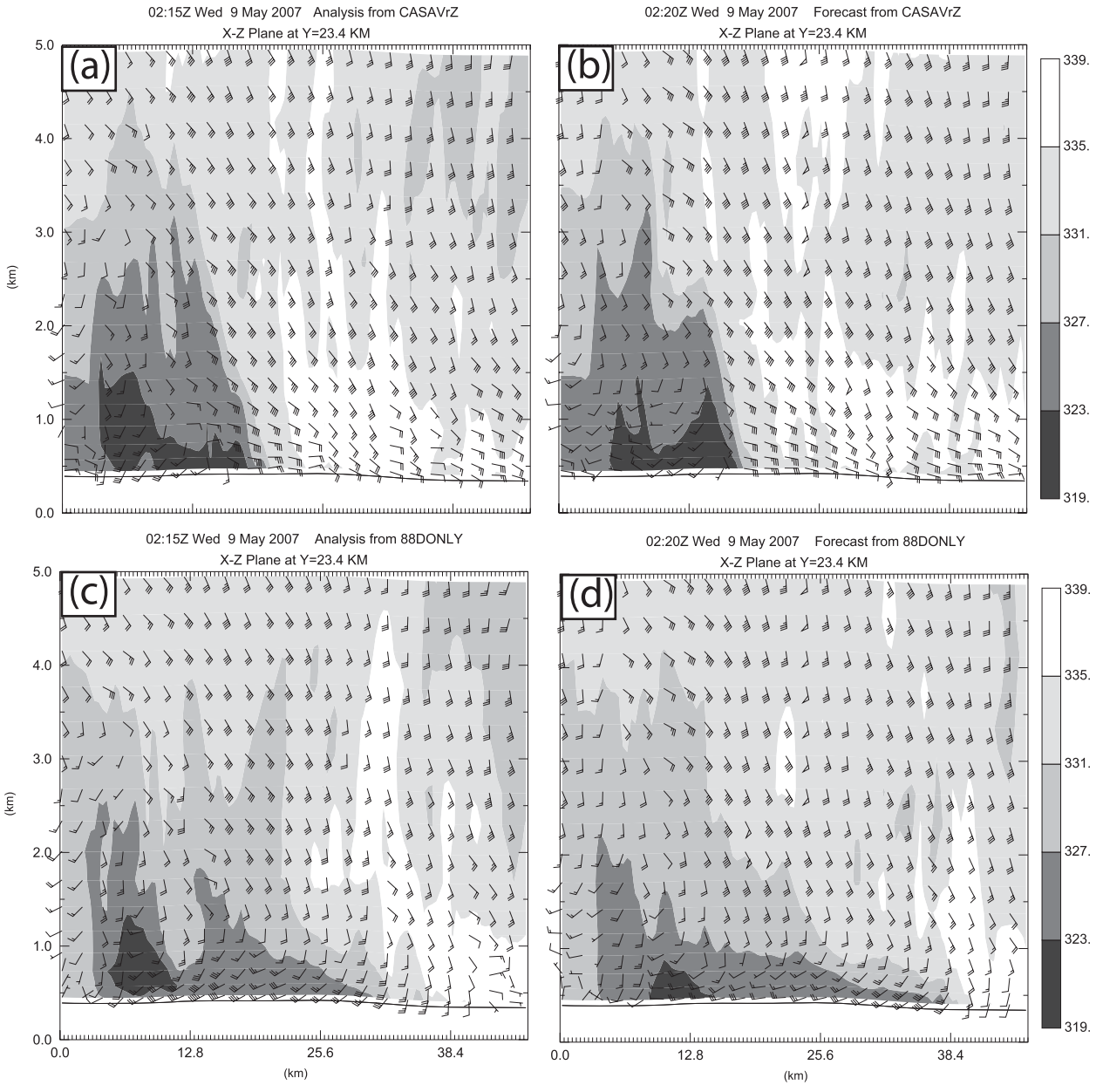

FIG. 6. East–west cross sections along the lines in Figs. 3a,b, of the analyses at (left) 0215 UTC and the forecasts at (right) 0220 UTC from experiments (top) CASAVrZ and (bottom) 88DONLY. Equivalent potential temperature is shaded at 4-K intervals and wind barbs are for horizontal winds in m s^{-1} (a full barb represents 5 m s^{-1}).

Thereafter, the forecast evolution becomes less correlated with the initial conditions, at least at the substorm scale, and depends more on the storm-scale and substorm-scale interactions within the model. As such, our discussion focuses predominantly on the forecast period before 0400 UTC. Forecast results after 0400 UTC are also discussed, but it is difficult to draw meaningful conclusions without a careful study of the related predictability issues, which is outside of the scope of this paper.

1) LLW EXPERIMENTS

Over the first 40 min of the forecast period in all experiments the secondary gust front moves southeast. In the LLW experiments, the primary cold pool spreads slowly to the east and weakens. This allows the secondary gust front to quickly overtake and merge with the primary gust front (Fig. 7). At 0300 UTC, the northern portion of the secondary gust front is marked by a sharp equivalent potential temperature θ_e gradient and substantial

low-level convergence between the secondary cold-pool air and environmental inflow to its east (Fig. 8).[1] A mesovortex forms along the northern portion secondary gust front (Fig. 9a) but dissipates quickly after 0300 UTC as the secondary gust front continues to surge east.

By 0315 UTC, a second, stronger, mesovortex has formed farther south in the LLW experiments. This mesovortex, like the initial mesovortex, has developed along the northern portion of the secondary gust front and is analogous to (and will be referred to hereafter as) the Minco mesovortex. The Minco mesovortex dissipates around 0405 UTC in extreme south-central Canadian County (cf. Fig. 1).

As in Weisman and Trapp (2003) and Atkins and St. Laurent (2009a), we examine the low-level shear to explain the behavior of the mesovortices. The initial mesovortex forms along the secondary gust front in an area of weak low-level shear (Fig. 9a). As a result of the weak low-level shear, the secondary gust front continues to surge quickly east, which inhibits the development of a persistent deep, upright updraft and leads to a mesovortex that is weak and short lived. In contrast, the Minco mesovortex forms as the secondary gust front encounters strong positive low-level shear ahead of it (Fig. 9b). This causes the secondary gust front to slow its eastward progress substantially and allows the Minco mesovortex to strengthen rapidly and persist for more than 40 min beneath a deep, persistent updraft (Fig. 10). Weisman and Trapp (2003) and Atkins and St. Laurent (2009a) suggest that a deep, persistent updraft was critical in the development of intense, long-lived mesovortices because of persistent stretching of vertical vorticity due to the updraft.

Following the dissipation of the simulated Minco mesovortex, an additional mesovortex forms in far southeastern Canadian County at 0420 UTC along the leading edge of the secondary gust front. This mesovortex is spurious as TDWR observations do not indicate such a feature. A final mesovortex forms near El Reno at 0440 UTC in CASAVrZ. This mesovortex forms in close proximity to the observed El Reno mesovortex. However, no additional mesovortices form in experiment CASAVr. Thus, owing to complicated storm-scale and substorm-scale interactions that are difficult to trace back to the initial conditions, it is difficult to determine whether the mesovortex in CASAVrZ is an accurate representation of the El Reno mesovortex, or whether it is simply a coincidental development.

2) NLLW EXPERIMENTS

The first 40 min of the forecast period in the NLLW experiments are characterized by the secondary gust front surging southeast, as in the LLW experiments. Unlike the LLW experiments, however, the primary gust front moves quickly to the northeast. As a result the secondary gust front remains behind the primary gust front (Fig. 11). This leads to much weaker convergence and baroclinicity along the secondary gust front in the NLLW experiments (e.g., cf. the convergence and θ_e gradient along the secondary gust front in Fig. 12 to that in Fig. 8). The lack of baroclinicity and convergence precludes mesovortex development along the secondary gust front in the NLLW experiments.

While no mesovortices develop along the secondary gust front in the NLLW experiments, sufficient convergence and baroclinicity for mesovortex development is present along the surging primary gust front in the NLLW experiments. As a result, between 0240 and 0300 UTC, at least 4 cyclonic mesovortices form along the primary gust front in the NLLW experiments. An example of these mesovortices in 88DONLY is shown in Fig. 13 (CASAZ is nearly identical to 88DONLY and is not shown). These mesovortices develop in a generally weak prefrontal positive low-level shear situation and are short lived, dissipating by 0330 UTC. Comparison with radial velocity observations indicates that the two southernmost of these mesovortices did not actually occur (Fig. 14). This serves to further validate our assertion that the gust front position and behavior in LLW experiments are more accurate than those of the NLLW experiments.

The other two of the four mesovortices in the NLLW experiments are located in a similar area as the initial and Minco mesovortices are in the LLW experiments; however, the simulated mesovortex in the area of the observed Minco mesovortex is much weaker and shorter lived than it was in the LLW experiments. Moreover, the forecast of these two mesovortices has large temporal errors, tracking in the vicinity of the observed initial and Minco mesovortex tracks at least 1 h earlier than observed. There is no mesovortex of comparable strength and longevity to the Minco mesovortex in the NLLW experiments. Weak circulations that form along the secondary gust front in the NLLW experiments do not persist or strengthen like those in the LLW experiments because the location of the primary gust front relative to the secondary gust front in the NLLW experiments

[1] As described in the introduction, Weisman and Trapp (2003) and Atkins and St. Laurent (2009b) found that such environments are favorable for mesovortex development. Thus, it is likely that the secondary outflow in this simulation is playing a similar role to the rear-inflow jet or convective-scale downdrafts described in those studies. However, determining the exact origin of the secondary outflow surge would require detailed analysis of the 2-km simulation results, which is beyond the focus of the present study.

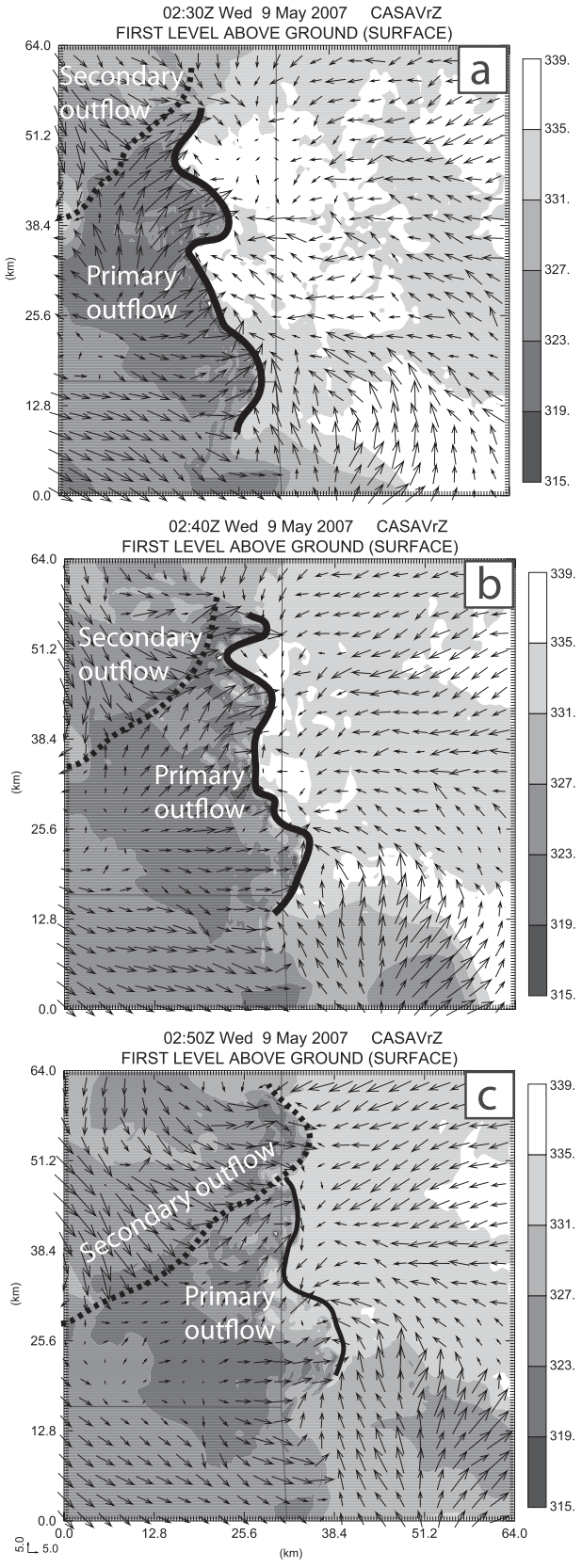

prevents the secondary gust front from overtaking the primary gust front. Thus, the secondary gust front never encounters the environmental inflow, which precludes the development of strong baroclinicity and convergence along the secondary gust front. Meanwhile, there is only weak positive low-level shear along and in advance of the primary gust front. Thus, there is a lack of strong, persistent, upright updrafts along both the surging primary and secondary gust fronts creating an unfavorable environment for strong, long-lived mesovortex development throughout the NLLW forecast period.

Figure 15 compares the observed base scan radial velocity from KOKC with simulated KOKC base radial velocity from CASAVrZ and 88DONLY at 0340 UTC. Though the Minco mesovortex in CASAVrZ is larger and more intense than observed with too much flow toward KOKC to the south of the Minco mesovortex, qualitatively, the general pattern closely resembles observations from KOKC. In contrast, the simulated radial velocity field from 88DONLY only vaguely resembles observations from KOKC.

As in the LLW experiments, the NLLW solutions diverge after 0400 UTC owing to complex storm-scale and substorm-scale interactions. In 88DONLY, no additional mesovortices form after 0330 UTC. In contrast, several additional mesovortices develop in CASAZ (not shown). The first of these mesovortices develops in south-central Canadian County at 0355 UTC. This mesovortex dissipates by 0420 UTC. Another mesovortex forms about 5 km north of the previous mesovortex at 0420 UTC. This mesovortex also dissipates after 20 min. A final mesovortex develops in extreme east central Canadian County at 0455 UTC and is ongoing at the end of the forecast period.

The NORAD experiment was conducted to show the degradation of results when radar data are not assimilated. As was presented in S11, the benefits of assimilating radar data are readily apparent when comparing the forecast from NORAD with the radar-assimilating experiments. The forecast from NORAD begins with numerous convective cells in the western half of the domain (Fig. 16a). With time these convective cells organize and grow upscale into a MCS (Fig. 16b). The MCS is poorly

←

FIG. 7. The near-surface forecast from experiment CASAVrZ at (a) 0230, (b) 0240, and (c) 0250 UTC. Equivalent potential temperature is shaded gray at 4-K intervals, vectors are for horizontal winds (m s^{-1}), and the heavy black line represents the approximate location of the primary gust front. The secondary gust front is marked by the heavy dashed line.

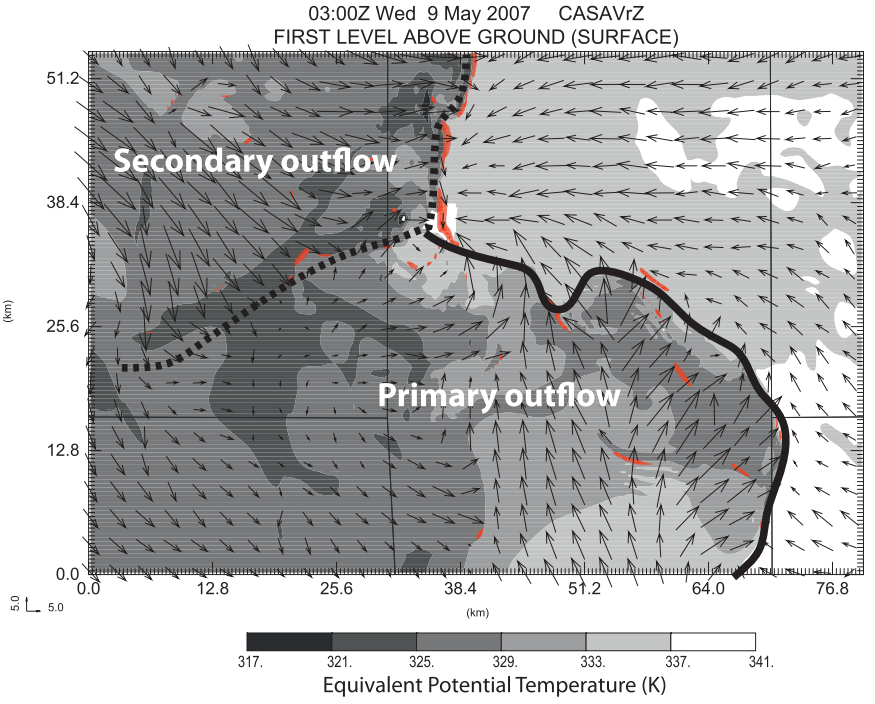

FIG. 8. The 0300 UTC forecast from experiment CASAVrZ. Equivalent potential temperature plotted as specified in Fig. 3 with the addition of near surface divergence (shaded in red where $\leq -1 \times 10^{-2}$ s^{-1}). The thick black line marks the location of the primary outflow gust front. The dotted line marks the location of the secondary gust front.

organized with no well-defined secondary gust front or LEV. As a result, mesovortices do not develop in NORAD.

3) FURTHER DISCUSSION AND A CONCEPTUAL MODEL

Figure 17 summarizes the discussion above by comparing observed mesovortex locations derived from KOKC radial velocity observations[2] with mesovortex locations from the various experiments. Note the clustering of mesovortex tracks near the observed Minco mesovortex from the LLW experiments in Fig. 17a. This clustering strongly suggests that the assimilated CASA radial velocity plays a vital role in the successful simulation of the Minco mesovortex. Figure 17b shows that in 88DONLY mesovortices tracked close to the observed Minco mesovortex; however, as noted in the previous subsection these forecast mesovortices were weak and short lived with large temporal errors.

Figure 18 presents a conceptual diagram of the secondary and primary gust front interaction for the LLW and NLLW experiments. As outlined above, assimilation of CASA radial velocity leads to a more accurate analysis of the low-level wind shear profile ahead of the primary convective cold pool, leading to favorable shear, baroclinicity, and convergence for mesovortex intensification along the secondary gust front during the forecast period when the surging secondary gust front overtakes the slow-moving, weaker primary gust front (Fig. 18a). Without the assimilation of CASA radial velocity data, the analyzed low-level front-normal shear is weak (and negative) ahead of the primary convective cold pool and associated gust front, which allows the primary gust front to surge too far to the east during the analysis and forecast periods. As a result, the secondary gust front remains behind the primary convective gust front, which precludes the secondary gust front from interacting with the prefrontal low-level shear flow thus leading to weaker shear, baroclinicity, and convergence along the secondary gust front (Fig. 18b). These conditions lead to a lack of mesovortex development along the secondary gust front in the NLLW experiments and instead, weak, short-lived mesovortices form in the weaker shear and baroclinicity along the primary gust front in the NLLW experiments. Thus, the overall impact of assimilating CASA Vr data in this case is to *indirectly* set up environmental conditions that are

[2] Positions were derived by visually determining and tracking the center of the cyclonic shear signature of the mesovortex.

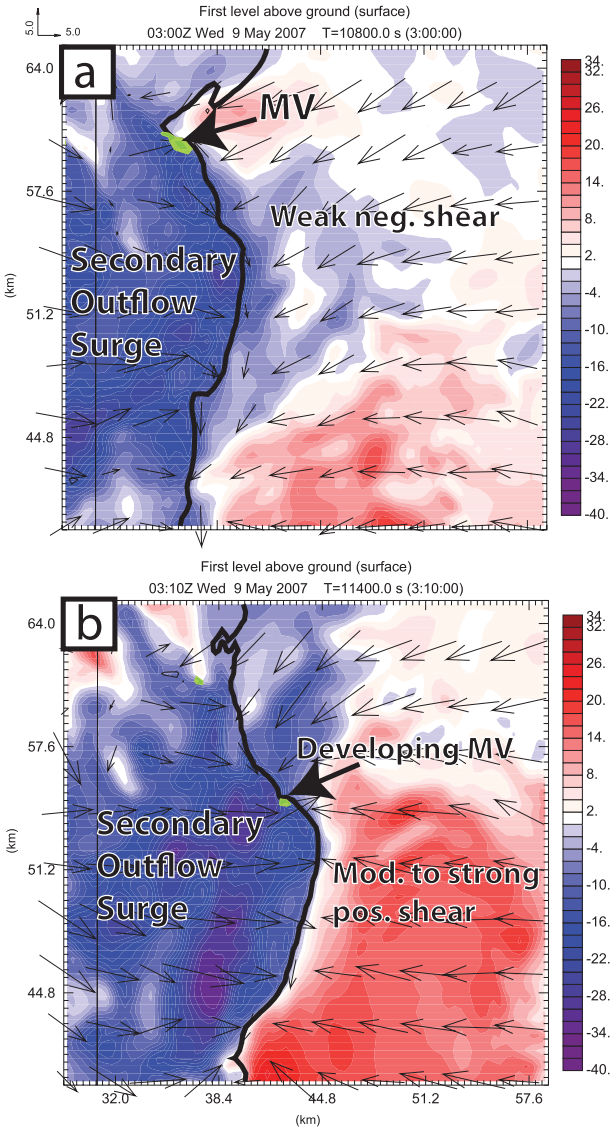

FIG. 9. Near-surface to 2.5 km AGL difference in magnitude of u-component velocity (shaded, m s^{-1}) and near-surface velocity vectors (m s^{-1}) from CASAVrZ at (a) 0300 and (b) 0310 UTC. The small green shading areas are for vertical vorticity exceeding 1.4×10^{-2} s^{-1}. The thick black curve represents the 334-K equivalent potential temperature contour that marks the approximate location of the gust front. The MV denotes mesovortex.

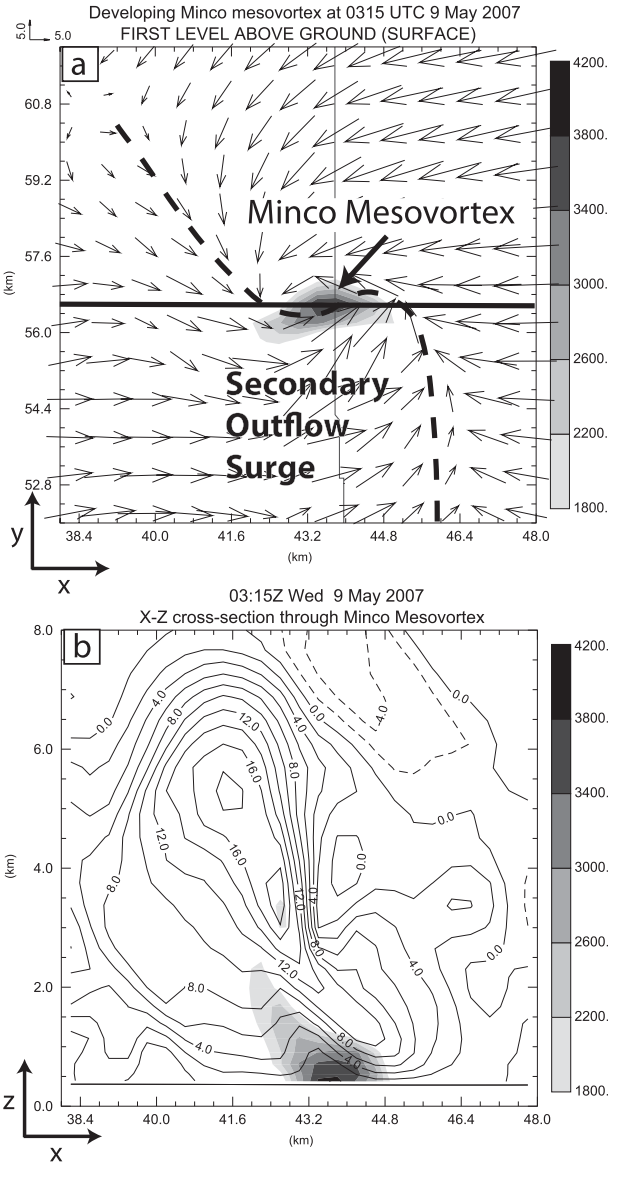

FIG. 10. (a) Horizontal wind and vorticity (shaded) at 0315 UTC 9 May 2007 from CASAVrZ and (b) x–z cross section through the developing Minco mesovortex along the thick black line in (a). The dashed line in (a) marks the locations of the secondary gust front. In (b) vertical velocity is contoured at 2 m s^{-1} intervals. In both (a) and (b), vertical vorticity is shaded at 400×10^{-5} s^{-1} intervals starting at 1800×10^{-5} s^{-1}.

favorable for long-lived mesovortex development by *directly* preventing the primary gust front from moving too far to the east in the analysis and early forecast period.

5. The impact of high-frequency Oklahoma Mesonet data

The experiments presented in this section examine the relative role of data from a mesoscale surface observation network and data from the CASA radars, both of which are available at (at least) 5-min intervals. Questions to answer include if the mesonet data can play as effective a role as the CASA low-level wind observations.

a. Analysis results

The 0220 UTC analysis from CASAVrZ5MM features a well-defined gust front with a similar orientation

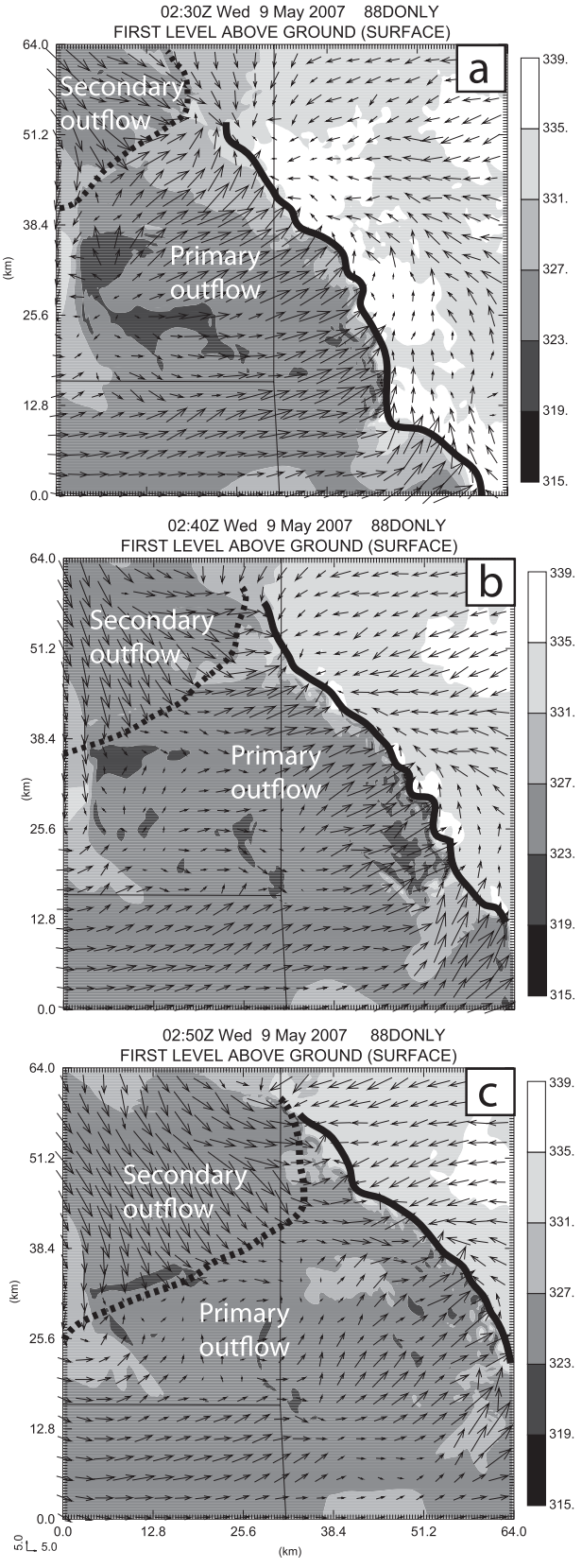

FIG. 11. As in Fig. 7, but for experiment 88DONLY.

and position to that of CASAVrZ (Figs. 19a,b). Only subtle differences exist between CASAVrZ5MM and CASAVrZ 0220 UTC analyses, indicating that the addition of 5-min Oklahoma Mesonet has little impact on the pertinent features. The only differences are in the low-level thermodynamic fields, manifested in θ_e values that are about 4 K higher in CASAVrZ5MM throughout the analysis domain. This difference is due to the fact that the Oklahoma Mesonet provides direct near-surface thermodynamic observations, information that cannot be provided by wind data alone as the 3DVAR formulation used here lacks cross covariances between state variables. The wind field analyses in Figs. 19a,b are virtually identical.

More significant differences exist when 5-min Oklahoma Mesonet observations are assimilated in experiment CASAZ5MM. Specifically, the easterly inflow in advance of the convective line is better resolved in the latter portions of the assimilation window in CASAZ5MM than in CASAZ (Fig. 20). By 0220 UTC, this leads to the gust front being located about 10 km farther west in CASAZ5MM than in CASAZ (Figs. 19c,d). The low-level easterly inflow also yields generally weak-to-moderate positive low-level shear ahead of the gust front in CASAZ5MM at 0220 UTC (Fig. 20c), suggesting a slower eastward movement in the latter analysis period. In CASAZ, the low-level shear ahead of the gust front, especially along the northern portion, generally remains weak (and negative) at 0220 UTC (Fig. 20d).

While the 5-min Oklahoma Mesonet data did lead to substantial differences between CASAZ5MM and CASAZ in the 0220 UTC analysis, the coarse resolution (mean spacing is about 30 km) of the Oklahoma Mesonet relative to that of the CASA radars prevents CASAZ5MM from fully resolving the strength and spatial extent of the easterly inflow that was well analyzed in the LLW experiments. As a result, the gust front in CASAZ5MM surges about 10 km farther east than the gust front in the LLW experiments by 0200 UTC, before slowing down as it encounters positive low-level shear after 0200 UTC. Thus, at the end of the assimilation window, the gust front in CASAZ5MM is about 10 km farther east and more diffuse than that of CASAVrZ5MM and the LLW experiments.

b. Forecast results

The substantial differences seen between CASAZ5MM and CASAZ in the analysis period lead to large improvements in the forecast of mesovortices in CASAZ5MM. As expected, the stronger positive low-level shear in the 0220 UTC analysis prevents the primary gust

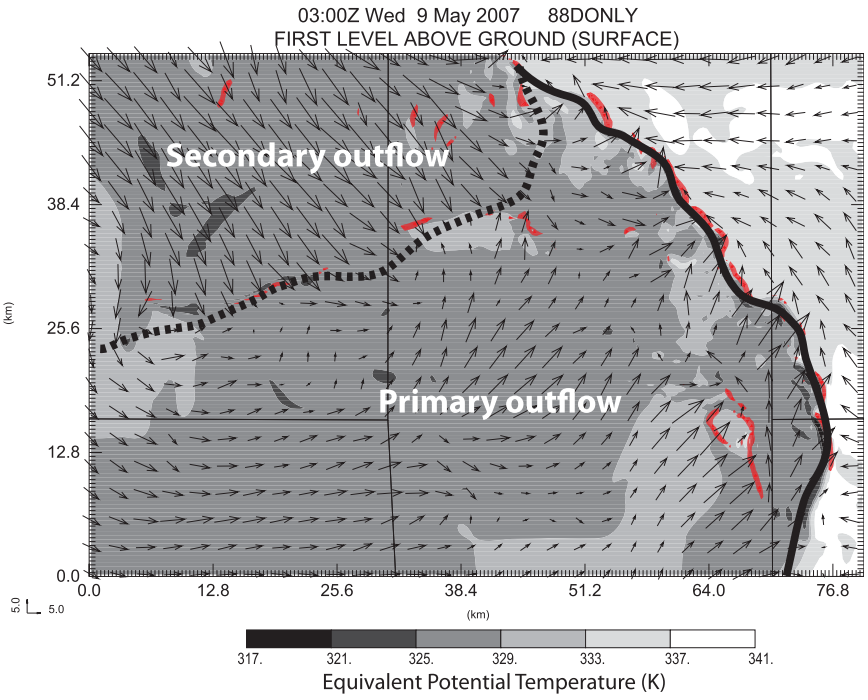

FIG. 12. As in Fig. 8, but for 88DONLY.

front from surging east in the forecast period of CASAZ5MM. As a result, the secondary gust front overtakes the primary gust front allowing sufficient positive low-level shear, baroclinicity, and convergence to develop along the secondary gust front for the development of a strong, long-lived mesovortex in a similar manner to the forecast Minco mesovortex in the LLW experiments.

While the assimilation of 5-min Oklahoma Mesonet data allowed for the forecasted development of the Minco mesovortex in CASAZ5MM, the Minco mesovortex develops approximately 15 min later and consequently about 10 km farther east than it does in the LLW experiments. This displacement occurs because the inability of the Oklahoma Mesonet to resolve the sharp gradient in the low-level shear profile along the primary gust front allows the primary gust front to move farther east in the analysis period, thus delaying the timing and shifting the location where the secondary gust front overtakes the primary gust front in the forecast period. Nonetheless, once the Minco mesovortex forms in CASAZ5MM it follows a similar evolution to the LLW experiments and dissipates around 0410 UTC approximately 10 km east of the dissipation location of the LLW experiments. This evolution represents a large improvement over CASAZ, in which no comparable mesovortex formed.

Following the dissipation of the Minco mesovortex, two additional mesovortices form in CASAZ5MM near the location of the observed El Reno mesovortex. The formation and evolution of these mesovortices is more similar to those of CASAVrZ than those of CASAZ indicating the environment in which they develop is likely more similar to CASAVrZ than that of CASAZ.

As expected from the 0220 UTC analysis, differences between CASAVrZ5MM and CASAVrZ (both assimilated Oklahoma Mesonet data but at 5-min and hourly frequencies, respectively) are much more subtle than those between CASAZ5MM and CASAZ. In fact, with the exception of slight differences in mesovortex position and timing, CASAVrZ5MM and CASAVrZ are nearly identical. In CASAVrZ5MM, as in CASAVrZ, a strong, long-lived mesovortex develops in the vicinity of the observed Minco mesovortex. Following the dissipation of this long-lived mesovortex, two additional mesovortices develop: one near Union City at 0410 UTC and another near El Reno at 0440 UTC. These additional mesovortices have 20-min life cycles and are weaker than the Minco mesovortex. Figure 21 shows the tracks of the mesovortices from CASAVrZ5MM and CASAZ5MM (cf. tracks in the experiments that do not assimilate 5-min mesonet data shown in Fig. 17). The spurious mesovortex that occurred in the LLW experiments in southeast Canadian county does not occur in CASAVrZ5MM, possibly suggesting that the assimilation of high-frequency Oklahoma Mesonet data leads to a

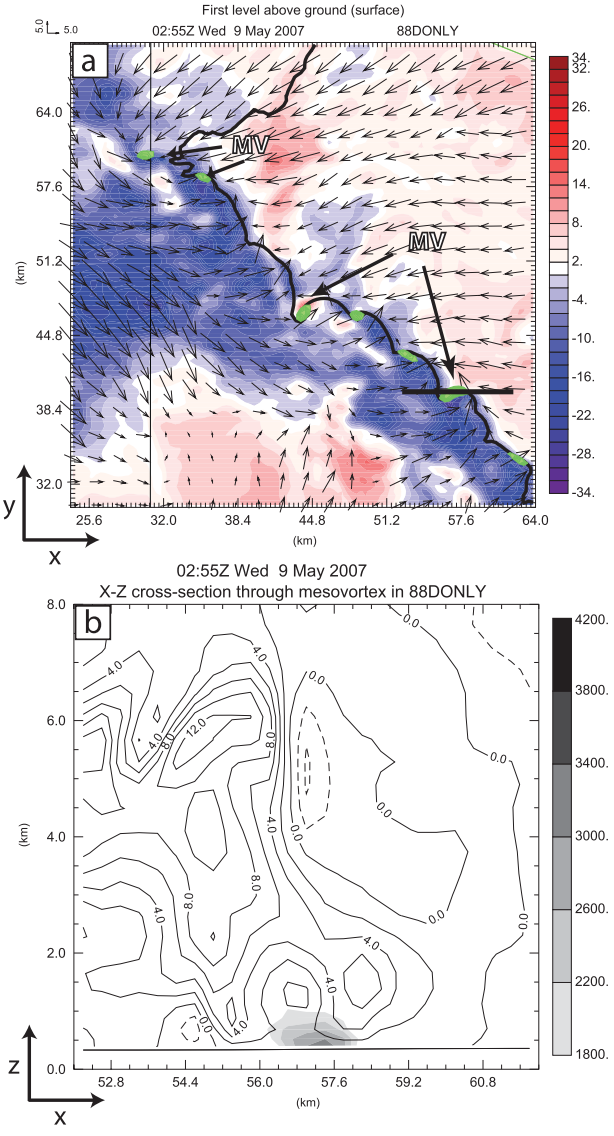

FIG. 13. (a) As in Fig. 9, but for 88DONLY at 0255 UTC and (b) x–z cross section along the thick black line in (a). "MV" marks vortices that meet the mesovortex criteria defined in the text. In (b) vertical velocity is contoured in 2 m s^{-1} intervals and vertical vorticity is shaded at 400 × 10^{-5} s^{-1} intervals starting at 1800 × 10^{-5} s^{-1}.

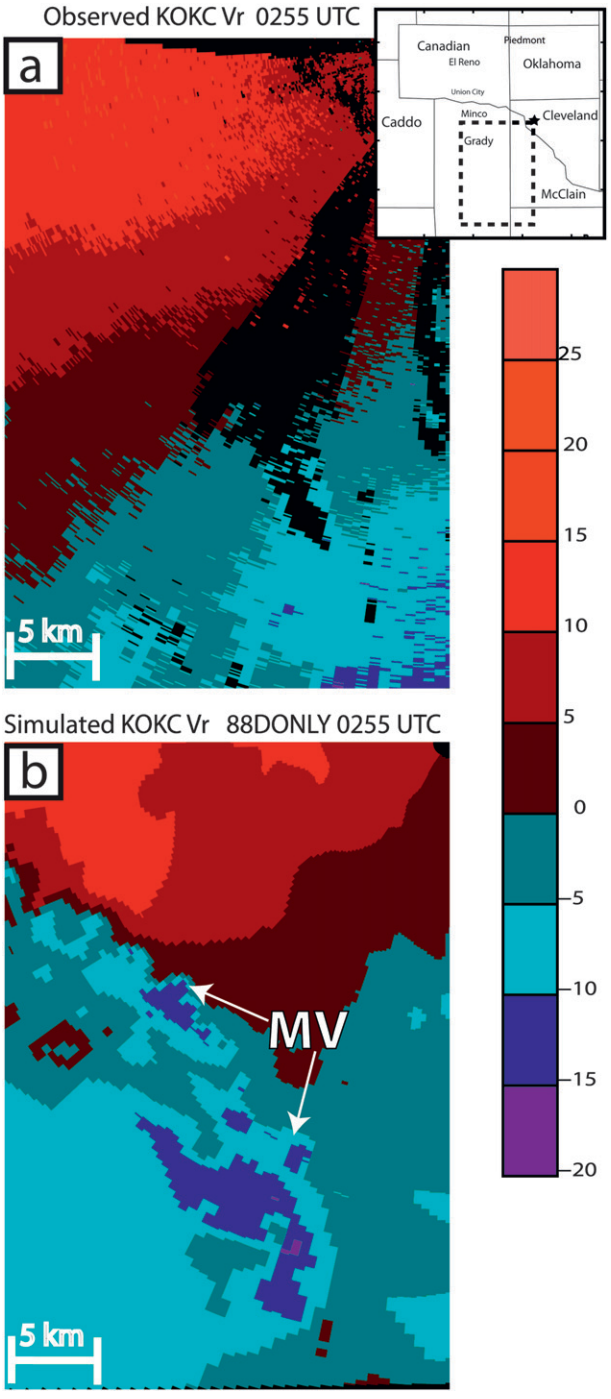

FIG. 14. Radial velocity (m s^{-1}) (a) observed from KOKC and (b) simulated for 88DONLY at 0255 UTC 9 May 2007. (a) Fields are plotted over the area marked by the dashed line rectangle in the map outset in the upper-right corner. "MV" marks mesovortices as determined in Fig. 13.

more accurate depiction of the environment. However, definitive assertions are difficult because complex storm interactions following the dissipation of the Minco mesovortex hinders straightforward attribution.

Overall, results suggest that high-frequency observations from the Oklahoma Mesonet have a positive impact on the analysis and forecast when high-resolution low-level wind observations from CASA are absent. This impact is lessened substantially when high-resolution CASAVr observations are assimilated along with the

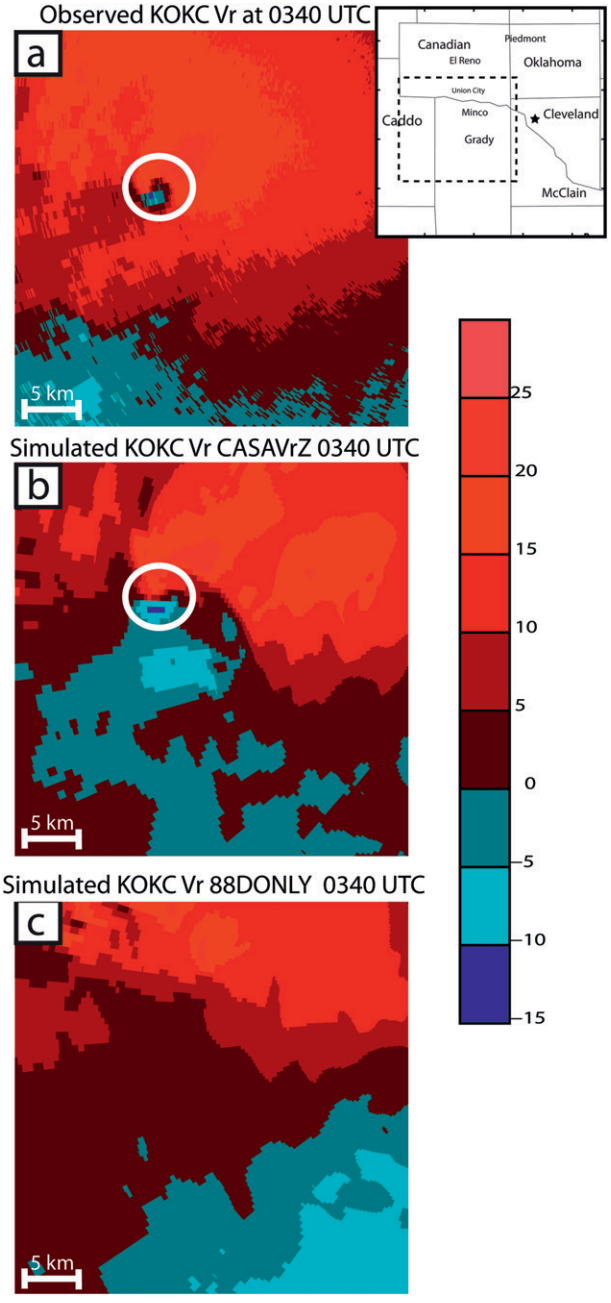

FIG. 15. As in Fig. 14, but at 0340 UTC (a) observed and simulated from (b) CASAVrZ and (c) 88DONLY. The white circle in (a),(b) has a diameter of 6 km and marks the location of the Minco mesovortex.

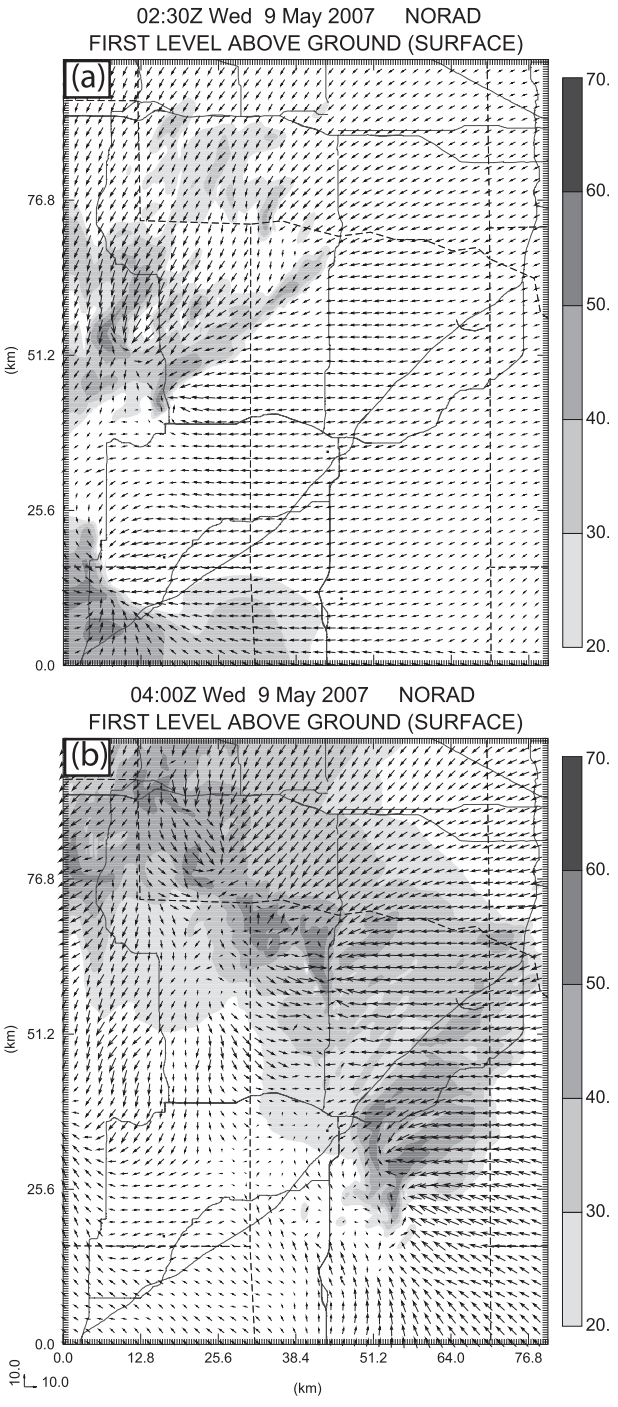

FIG. 16. Forecast radar reflectivity (shaded in dBZ) and horizontal wind vectors at the surface from NORAD at (a) 0230 and (b) 0400 UTC 9 May 2007.

Oklahoma Mesonet data. We also find that while Oklahoma Mesonet observations lead to substantial improvements in the forecast, these improvements are smaller than those realized from assimilating high-resolution CASAVr observations, which are available at spatial resolutions that are one to two orders of magnitude greater than the resolution of the Oklahoma Mesonet data. This allows CASA radars to observe detailed storm-scale and substorm-scale wind features, such as the sharp wind shift associated with the gust front in the present case, which the Oklahoma Mesonet typically cannot resolve.

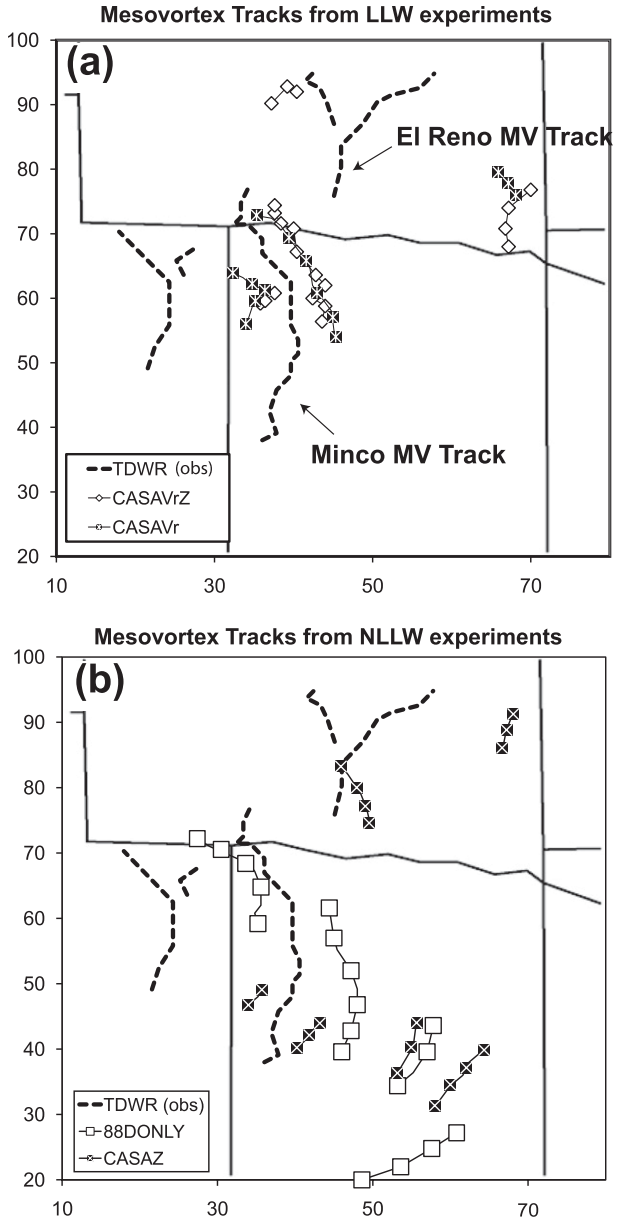

FIG. 17. Mesovortex tracks from the (a) LLW experiments and (b) NLLW experiments. Dashed lines without markers are mesovortex tracks derived from the KOKC TDWR. Markers correspond to experiments as indicated in the legend.

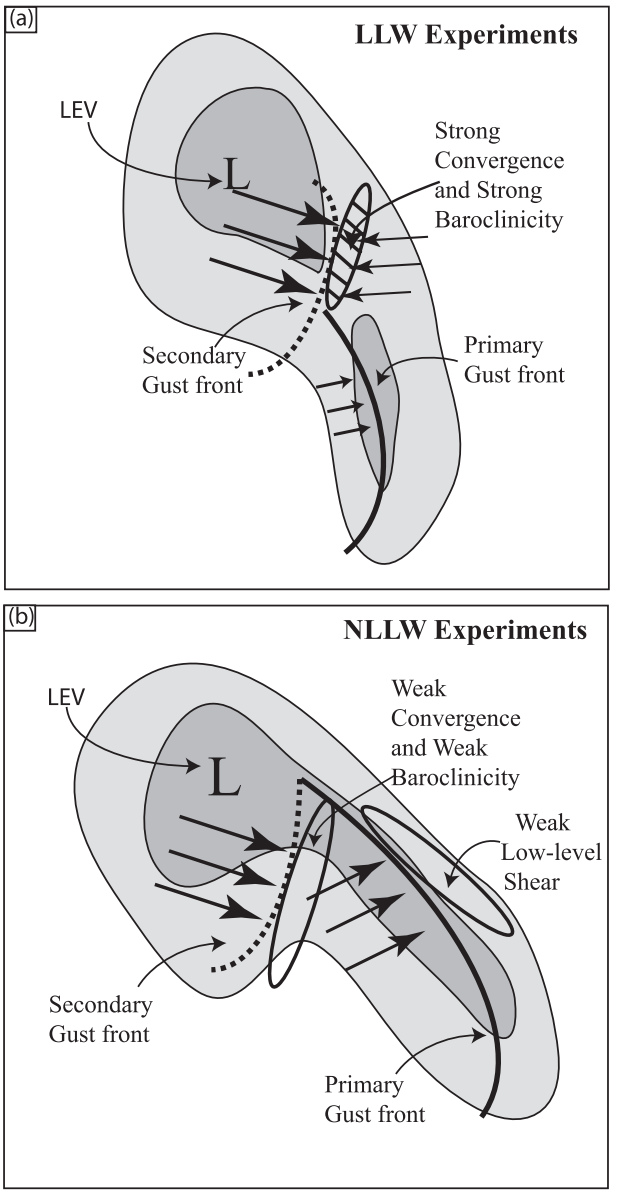

FIG. 18. A conceptual model summarizing the impact of assimilating low-level wind information from radar radial velocity data (or the lack thereof) on the forecast evolution of the primary and secondary gust fronts (and associated wind field) from (a) LLW and (b) NLLW assimilation experiments. Light and dark shading represents active convective and stratiform regions of the MCS, respectively. The hashed elliptical area in (a) marks the region favorable for the development of long-lived mesovortices owing to strong baroclinicity and strong convergence where the secondary gust front overtakes the primary gust front. The unfilled elliptical regions in (b) marks areas of weak low-level shear and weak convergence–baroclinicity along the primary and secondary gust front, respectively, in the NLLW experiments. These areas are unfavorable for the development of long-lived mesovortices.

6. Summary and conclusions

Recent studies (e.g., Weisman and Trapp 2003; Atkins et al. 2004; Atkins and St. Laurent 2009a) have shown that mesovortices are typically the parent circulation of tornadoes that occur within bow echoes and quasi-linear convective systems. These studies also have shown that damaging and/or tornadic mesovortices occur only when environmental shear is strong enough to

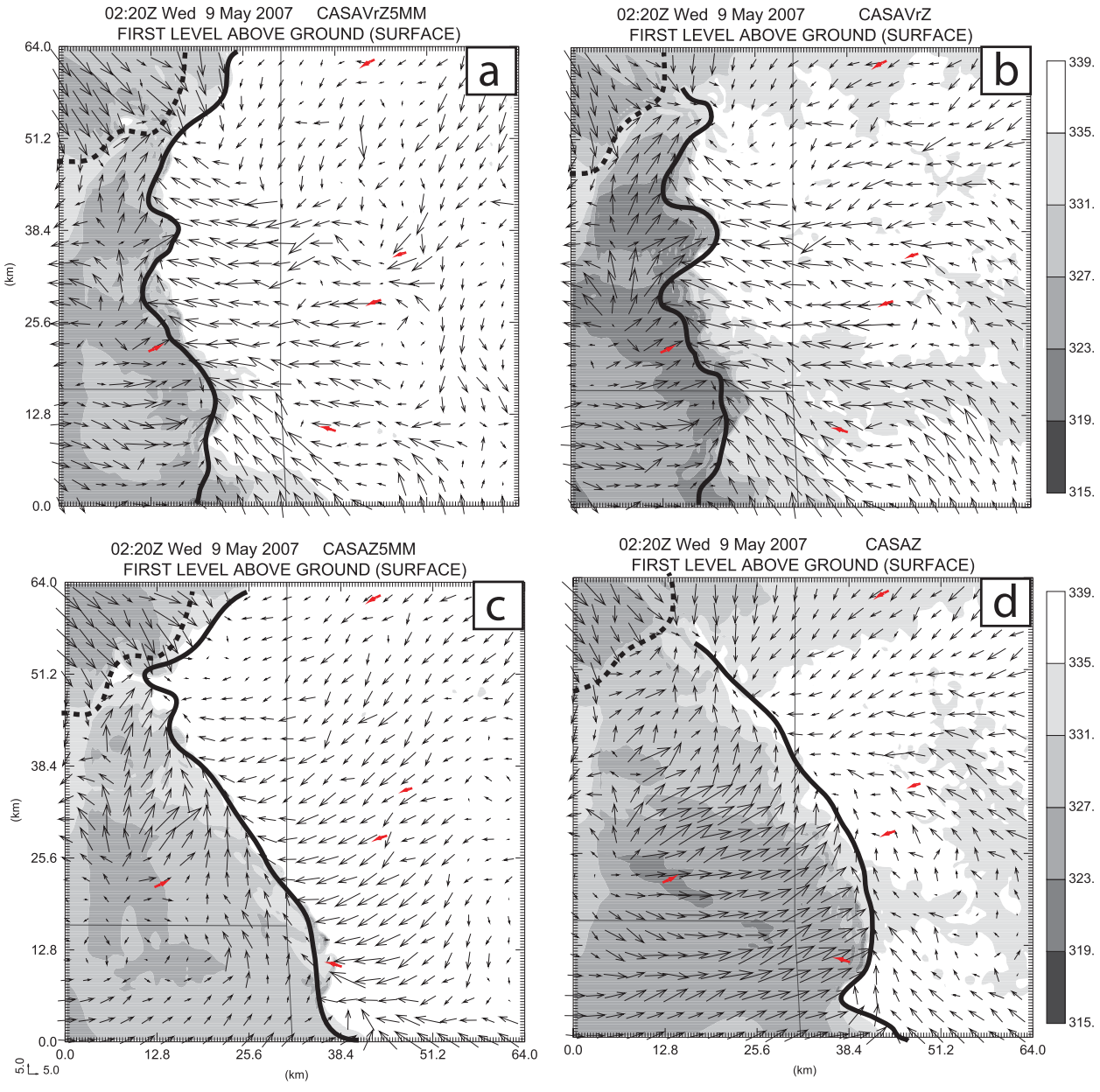

FIG. 19. As in Fig. 3, but for (a) CASAVrZ5MM, (b) CASAVrZ, (c) CASAZ5MM, and (d) CASAZ.

maintain vigorous, upright updrafts. Thus, in order to forecast these strong, long-lived mesovortices we hypothesized that it was necessary to resolve strong low-level shear in our assimilation system.

Experiments were designed to test our hypothesis by examining the impact of CASAVr and high-frequency Oklahoma Mesonet data on the accuracy of the overall analysis and the subsequent prediction of mesovortices. A 400-m resolution grid was nested within the 2-km grid for the 8–9 May 2007 Oklahoma tornadic mesoscale convective system. The 2-km simulations were reported in S11. The increased resolution made it possible to resolve substorm-scale mesovortices embedded within the system. The evolution, location, and timing of the predicted mesovortices from the experiments were qualitatively compared to mesovortices observed by the Oklahoma City TDWR in an attempt to determine which experiment(s) produced the most accurate forecast.

A key result of this study is the large positive impact of CASA radial velocity data on the analysis and subsequent prediction of the low-level wind fields and gust

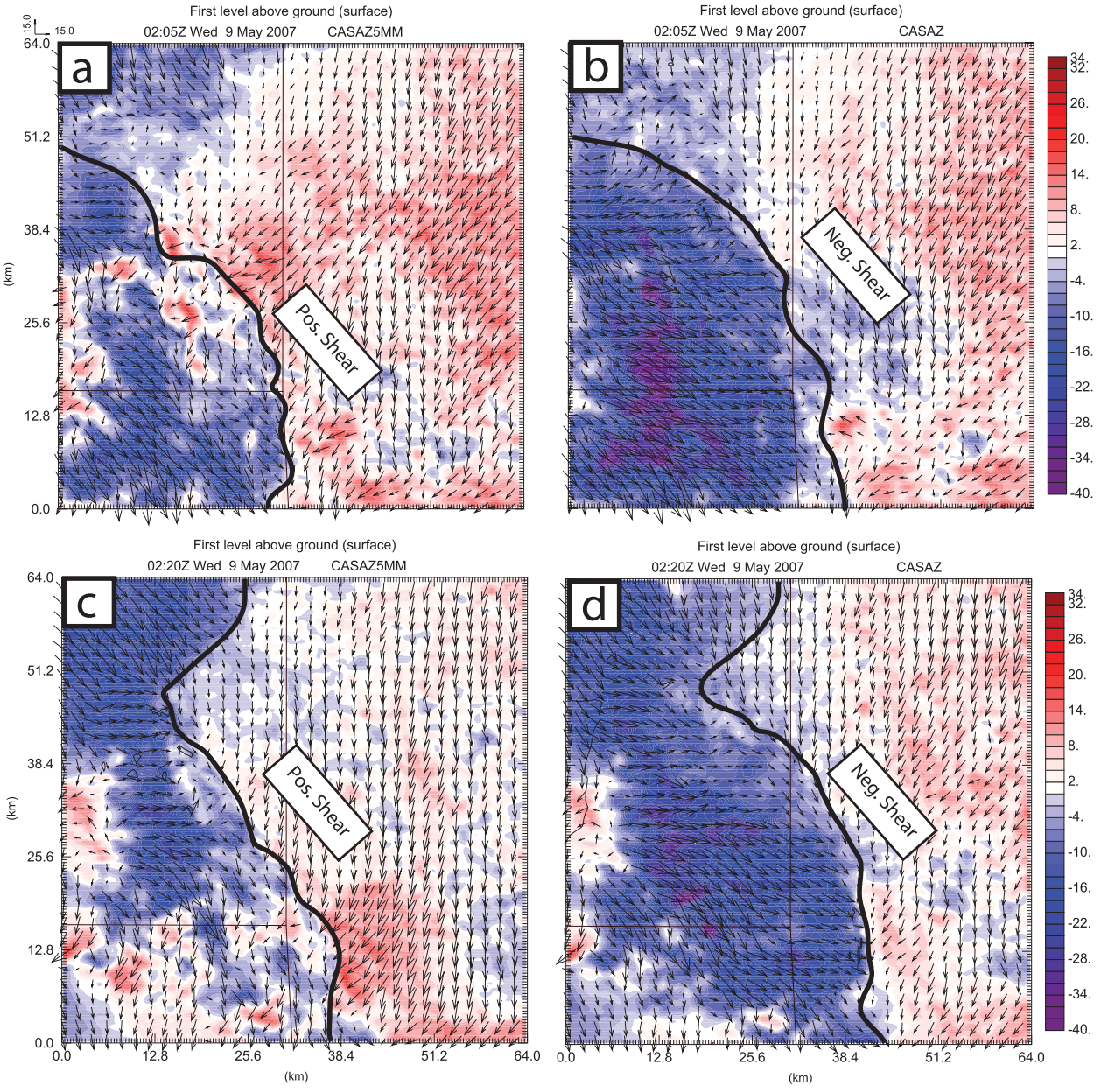

FIG. 20. As in Fig. 5, but at 0205 UTC for (a) CASAZ5MM and (b) CASAZ and 0220 UTC for (c) CASAZ5MM and (d) CASAZ.

fronts. Results presented in S11 also showed a positive impact from assimilating CASA radial velocity data on the prediction of the mesoscale features in this case. However, this impact was small and did not affect the development (or lack thereof) of the LEV. In contrast, at the higher resolution presented in this study, CASA radial velocity data led to significant improvements in the analyzed low-level winds in advance of the cold pool and gust front. These improvements continued into the forecast portion of the experiments, manifested in more favorable near-storm low-level shear and baroclinicity for the development of strong, long-lived mesovortices compared to experiments that did not assimilate CASA radial velocity data. In experiments that assimilated CASAVr data, a strong, long-lived mesovortex developed within 15 min and tracked within 5 km of the observed Minco mesovortex. Experiments that did not assimilate such data did not produce a comparable long-lived mesovortex. Given the tendency of strong, long-lived mesovortices to produce severe weather, the differences between these two groups of experiments are particularly noteworthy.

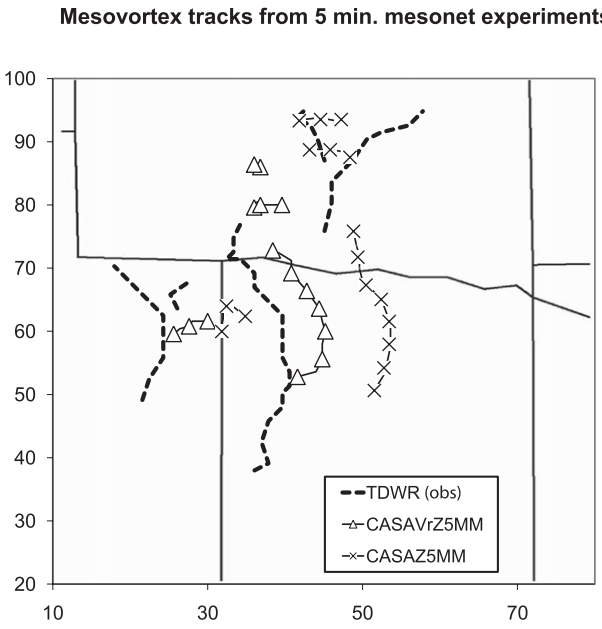

FIG. 21. As in Fig. 17, but for experiments that assimilate 5-min data from the Oklahoma Mesonet.

The assimilation of high-frequency (5 min) low-level wind information from the Oklahoma Mesonet also led to improvements in the analyzed near-storm environmental low-level wind profile. These improvements in the analyzed low-level wind profile led to the development of a long-lived mesovortex in the forecast from this experiment. However, because the Oklahoma Mesonet was unable to fully resolve the sharp wind shift along the gust front, experiments that did not assimilate CASA Vr data produced greater mesovortex track errors than in experiments that did assimilate CASA Vr.

The improvement due to CASA Vr assimilation has broad implications beyond the present study. Accurate analysis and prediction of the low-level cold pool and surface wind field are very important for the accurate prediction of most convective systems as a result of their active dynamic role in storm system development and evolution. Thus, the results presented herein suggest it may be possible to forecast storm-scale and substorm-scale features with good accuracy given adequate low-level wind information for assimilation.

It can be noted that the experiments presented herein do not have high enough resolution to explicitly simulate tornadoes. Additionally, it cannot be said that with increased resolution the predicted mesovortices would spawn tornado-like vortices. Nonetheless, the similarities between observations and the simulated Minco mesovortex and surrounding environment suggest that with increased resolution it may be possible to investigate tornadogenesis. Even higher-resolution nested grid simulations capable of resolving tornado-like vortices are planned to explore this issue. Moreover, the formation of the long-lived mesovortices in the model forecast at least indicates higher tornadogenesis potentials at those locations than otherwise. In practice, ensemble forecasting will be necessary to assess the forecast uncertainties (Stensrud et al. 2009).

Our study suggests a number of questions for future investigation. First, it should be determined if the results of this case generally apply in other cases, and for other types of convective systems such as supercells and severe squall lines. To accomplish this, additional CASA cases should be studied using similar methodologies to those presented herein. Also, the specific conclusions may be dependent on the data assimilation methods used. Parallel efforts are under way to help determine if the conclusions found here about the necessity of assimilating low-level wind observations in a 3DVAR framework extend to the more advanced ensemble Kalman filter data assimilation method.

Acknowledgments. This work was primarily supported by NSF Grant EEC-0313747, as part of ERC CASA. Partial support was also provided by AGS-0802888 and AGS-0738370. Ming Xue was also supported by NSF Grants ATM-0608168, ATM-0 750790, ATM-0941491, and OCI-0905040. Thanks to Matt Kumjian for a thorough review of this manuscript. Comments from three anonymous reviewers also helped strengthen this manuscript. Oklahoma Mesonet data are

provided courtesy of the Oklahoma Mesonet, a cooperative venture between Oklahoma State University and the University of Oklahoma and supported by the taxpayers of Oklahoma. The computing for this project was performed at the OU Supercomputing Center for Education & Research (OSCER) at the University of Oklahoma (OU).

REFERENCES

Atkins, N. T., and M. St. Laurent, 2009a: Bow echo mesovortices. Part I: Processes that influence their damaging potential. *Mon. Wea. Rev.,* **137,** 1497–1513.

——, and ——, 2009b: Bow echo mesovortices. Part II: Their genesis. *Mon. Wea. Rev.,* **137,** 1514–1532.

——, J. M. Arnott, R. W. Przybylinski, R. A. Wolf, and B. D. Ketcham, 2004: Vortex structure and evolution within bow echoes. Part I: Single-Doppler and damage analysis of the 29 June 1998 derecho. *Mon. Wea. Rev.,* **132,** 2224–2242.

——, C. S. Bouchard, R. W. Przybylinski, R. J. Trapp, and G. Schmocker, 2005: Damaging surface wind mechanisms within the 10 June 2003 Saint Louis bow echo during BAMEX. *Mon. Wea. Rev.,* **133,** 2275–2296.

Davis, C., and Coauthors, 2004: The Bow Echo and MCV Experiment: Observations and opportunities. *Bull. Amer. Meteor. Soc.,* **85,** 1075–1093.

Dowell, D., F. Zhang, L. J. Wicker, C. Snyder, and N. A. Crook, 2004: Wind and temperature retrievals in the 17 May 1981 Arcadia, Oklahoma, supercell: Ensemble Kalman filter experiments. *Mon. Wea. Rev.,* **132,** 1982–2005.

Forbes, G. S., and R. M. Wakimoto, 1983: A concentrated outbreak of tornadoes, downbursts and microbursts, and implications regarding vortex classification. *Mon. Wea. Rev.,* **111,** 220–235.

Fujita, T. T., 1978: Manual of downburst identification for Project Nimrod. SMRP Research Paper 156, The University of Chicago, 104 pp.

Funk, T. W., K. E. Darmofal, J. D. Kirkpatrick, V. L. DeWald, R. W. Przybylinski, G. K. Schmocker, and Y.-J. Lin, 1999: Storm reflectivity and mesocyclone evolution associated with the 15 April 1994 squall Line over Kentucky and Southern Indiana. *Wea. Forecasting,* **14,** 976–993.

Gao, J.-D., M. Xue, K. Brewster, and K. K. Droegemeier, 2004: A three-dimensional variational data analysis method with recursive filter for Doppler radars. *J. Atmos. Oceanic Technol.,* **21,** 457–469.

Hu, M., M. Xue, and K. Brewster, 2006a: 3DVAR and cloud analysis with WSR-88D level-II data for the prediction of Fort Worth tornadic thunderstorms. Part I: Cloud analysis and its impact. *Mon. Wea. Rev.,* **134,** 675–698.

——, ——, J. Gao, and K. Brewster, 2006b: 3DVAR and cloud analysis with WSR-88D level-II data for the prediction of Fort Worth tornadic thunderstorms. Part II: Impact of radial velocity analysis via 3DVAR. *Mon. Wea. Rev.,* **134,** 699–721.

Klemp, J. B., and R. Rotunno, 1983: A study of the tornadic region within a supercell thunderstorm. *J. Atmos. Sci.,* **40,** 359–377.

——, R. B. Wilhelmson, and P. S. Ray, 1981: Observed and numerically simulated structure of a mature supercell thunderstorm. *J. Atmos. Sci.,* **38,** 1558–1580.

McLaughlin, D., and Coauthors, 2009: Short-wavelength technology and the potential for distributed networks of small radar systems. *Bull. Amer. Meteor. Soc.,* **90,** 1797–1817.

Orlanski, I., 1975: A rational subdivision of scales for atmospheric processes. *Bull. Amer. Meteor. Soc.,* **56,** 527–530.

Pfost, R. L., and A. E. Gerard, 1997: ''Bookend vortex'' induced tornadoes along the Natchez Trace. *Wea. Forecasting,* **12,** 572–580.

Przybylinski, R. W., 1995: The bow echo: Observations, numerical simulations, and severe weather detection methods. *Wea. Forecasting,* **10,** 203–218.

Rotunno, R., 1993: Supercell thunderstorm modeling and theory. *The Tornado: Its Structure, Dynamics, Hazards, and Prediction, Geophys. Monogr.,* Vol. 79, Amer. Geophys. Union, 57–73.

——, J. B. Klemp, and M. L. Weisman, 1988: A theory for strong long-lived squall lines. *J. Atmos. Sci.,* **45,** 463–485.

Schenkman, A., M. Xue, A. Shapiro, K. Brewster, and J. Gao, 2011: The analysis and prediction of the 8–9 May 2007 Oklahoma tornadic mesoscale convective system by assimilating WSR-88D and CASA radar data using 3DVAR. *Mon. Wea. Rev.,* **139,** 224–246.

Skamarock, W. C., M. L. Weisman, and J. B. Klemp, 1994: Three-dimensional evolution of simulated long-lived squall lines. *J. Atmos. Sci.,* **51,** 2563–2584.

Snook, N., M. Xue, and Y. Jung, 2011: Analysis of a tornadic mesoscale convective vortex based on ensemble Kalman filter assimilation of CASA X-band and WSR-88D radar data. *Mon. Wea. Rev.,* **139,** 3446–3468.

Stensrud, D. J., and Coauthors, 2009: Convective-scale warn-on-forecast system: A vision for 2020. *Bull. Amer. Meteor. Soc.,* **90,** 1487–1499.

Sun, J., 2005: Initialization and numerical forecasting of a supercell storm observed during STEPS. *Mon. Wea. Rev.,* **133,** 793–813.

Trapp, R. J., S. A. Tessendorf, E. S. Godfrey, and H. E. Brooks, 2005: Tornadoes from squall lines and bow echoes. Part I: Climatological distribution. *Wea. Forecasting,* **20,** 23–34.

Wakimoto, R. M., H. V. Murphey, A. Nester, D. P. Jorgensen, and N. T. Atkins, 2006a: High winds generated by bow echoes. Part I: Overview of the Omaha bow echo 5 July 2003 storm during BAMEX. *Mon. Wea. Rev.,* **134,** 2793–2812.

——, ——, C. A. Davis, and N. T. Atkins, 2006b: High winds generated by bow echoes. Part II: The relationship between the mesovortices and damaging straight-line winds. *Mon. Wea. Rev.,* **134,** 2813–2829.

Weisman, M. L., 1993: The genesis of severe long-lived bow-echoes. *J. Atmos. Sci.,* **50,** 645–670.

——, and C. A. Davis, 1998: Mechanisms for the generation of mesoscale vortices within quasi-linear convective systems. *J. Atmos. Sci.,* **55,** 2603–2622.

——, and R. J. Trapp, 2003: Low-level mesovortices within squall lines and bow echoes. Part I: Overview and dependence on environmental shear. *Mon. Wea. Rev.,* **131,** 2779–2803.

Wicker, L. J., and R. B. Wilhelmson, 1995: Simulation and analysis of tornado development and decay within a three-dimensional supercell thunderstorm. *J. Atmos. Sci.,* **52,** 2675–2703.

Xu, Q., 1992: Density currents in shear flows—A two-fluid model. *J. Atmos. Sci.,* **49,** 511–524.

——, M. Xue, and K. K. Droegemeier, 1996: Numerical simulations of density currents in sheared environments within a vertically confined channel. *J. Atmos. Sci.,* **53,** 770–786.

Xue, M., K. K. Droegemeier, V. Wong, A. Shapiro, and K. Brewster, 1995: ARPS version 4.0 user's guide. Center for Analysis and Prediction of Storms, University of Oklahoma, 380 pp. [Available at http://www.caps.ou.edu/ARPS.]

——, Q. Xu, and K. K. Droegemeier, 1997: A theoretical and numerical study of density currents in non-constant shear flows. *J. Atmos. Sci.,* **54,** 1998–2019.

——, K. K. Droegemeier, and V. Wong, 2000: The Advanced Regional Prediction System (ARPS)—A multiscale nonhydrostatic atmospheric simulation and prediction tool. Part I: Model dynamics and verification. *Meteor. Atmos. Phys.,* **75,** 161–193.

——, and Coauthors, 2001: The Advanced Regional Prediction System (ARPS)—A multi-scale nonhydrostatic atmospheric simulation and prediction tool. Part II: Model physics and applications. *Meteor. Atmos. Phys.,* **76,** 143–166.

——, D.-H. Wang, J.-D. Gao, K. Brewster, and K. K. Droegemeier, 2003: The Advanced Regional Prediction System (ARPS), storm-scale numerical weather prediction and data assimilation. *Meteor. Atmos. Phys.,* **82,** 139–170.